Czech Technical University in Prague
Faculty of Nuclear Sciences and Physical Engineering

Measurement of inclusive jet p_{T} spectra in $\mathrm{p}+\mathrm{p}$ collisions at ALICE

Měření inkluzivních p_{T} spekter jetů ve srážkách $\mathrm{p}+\mathrm{p}$ na experimentu ALICE

Master's Thesis

Author:	**Bc. Peter Príbeli**
Supervisor:	**RNDr. Filip Křížek, Ph.D.**
Academic year:	2017/2018

- Zadání práce -

- Zadání práce (zadní strana) -

Acknowledgement:

I would like to thank Filip Křížek for his expert guidance and express my gratitude to my family for their loving support.

Author's declaration:

I declare that this Master's Thesis is entirely my own work and I have listed all the used sources in the bibliography.

I authorise the use of this work in accordance with § 60 of Law No. 121/2000 Coll. on Copyright, Rights Related to Copyright and on the Amendment of Certain Laws (Copyright Act) of the Czech Republic.

Prague, the 4th of May, 2018 Peter Príbeli

Název práce:

Měření inkluzivních p_T spekter jetů ve srážkách p+p na experimentu ALICE

Autor: Bc. Peter Príbeli

Obor: Experimentální jaderná a částicová fyzika

Druh práce: Diplomová práce

Vedoucí práce: RNDr. Filip Křížek, Ph.D., Ústav jaderné fyziky AV ČR, v.v.i.

Abstrakt: Práce pojednává o měření inklusivního p_T spektra nabitých, antik_T jetů s $R = 0.4$ ve srážkách proton-proton $\sqrt{s} = 13$ TeV. V úvodu se věnujeme problematice popisu tvrdých procesů ve srážkách $\mathrm{p+p}$ a základním principům kvantové chromodynamiky. Následně je podán popis experimentu ALICE. V analyzační části shrnujeme kritéria na výběr případů, drah částic a jetů a odhadujeme systematické chyby měření. Naměřené inklusivní p_T spektrum nabitých jetů korigované na detektorové efekty je porovnáno s předpovědí modelu PYTHIA8 Tune 4C a JEWEL.

Klíčová slova: anti-k_T jet algoritmus, jet, QCD, SVD dekonvoluce, silná interakce, tvrdý proces

Title:

Measurement of inclusive jet p_T spectra in $\mathrm{p+p}$ collisions at ALICE

*Author:*Bc. Peter Príbeli

Abstract: The thesis reports on the measurement of inclusive p_T spectra of charged, anti-k_T jets with $R = 0.4$ in proton-proton collisions at $\sqrt{s} = 13$ TeV. The first part concerns the description of hard processes in $\mathrm{p+p}$ collisions and the basic principles of Quantum Chromodynamics. Then the description of the ALICE experiment is put forth. In the analysis part of the thesis the criteria for event, track and jet selection are stated and systematic uncertainties of the measurement are estimated. The measured inclusive p_T spectra of charged jets corrected for detector effects is compared with predictions of the model obtained using PYTHIA8 Tune 4C and JEWEL.

Key words: anti-k_T jet algorithm, hard process, jet, QCD, SVD unfolding, Strong interaction

Contents

Introduction **13**

1 Hard scattering processes in p+p **15**

1.1 Cross-sections . . . 15
1.2 The QCD Lagrangian . . . 16
1.3 Elementary QCD cross-sections . . . 16
1.4 Asymptotic freedom . . . 18
1.5 Parton distribution functions . . . 20
1.6 Confinement . . . 22
1.7 Jets . . . 24
1.8 Background subtraction . . . 27
  1.8.1 Standard area based approach . . . 28
  1.8.2 CMS background . . . 28
  1.8.3 Perpendicular cone background . . . 28
1.9 p+p jet p_{T} spectra measurements in ALICE . . . 29

2 Experimental setup **31**

2.1 The Large Hadron Collider . . . 31
2.2 A Large Ion Colliding Experiment . . . 31
  2.2.1 Inner Tracking System (ITS) . . . 34
  2.2.2 Time Projection Chamber (TPC) . . . 34
  2.2.3 V0 . . . 34
  2.2.4 Computational infrastructure . . . 34

3 Analysis of p_{T} spectra of inclusive charged jets in p+p collisions at $\sqrt{s} = 13$ TeV **37**

3.1 Event selection . . . 37
3.2 Track selection . . . 38
3.3 Jet selection . . . 40
3.4 Data quality assurance . . . 40
  3.4.1 Period *2015f* . . . 41
  3.4.2 Period *2016l* . . . 42

4 Analysis of simulations **45**

4.1 Simulated events anchored to runs from *2016l* . . . 45

5 Raw jet p_{T} spectra **51**

6 Unfolding 55
6.1 Singular Value Decomposition . . . 55
6.2 Response matrix . . . 56
6.3 Results . . . 58
6.4 Closure test . . . 62

7 Systematic uncertainties 65
7.1 Unfolding algorithm and regularisation parameter . . . 65
7.2 Choice of the prior spectrum . . . 67
7.3 Binning . . . 68
7.4 Track reconstruction efficiency . . . 68
7.5 Momentum smearing . . . 69
7.6 Total systematic uncertainties . . . 73

8 Comparison of the final spectrum to the predictions of MC generators 77

Conclusion and Outlook 79

List of Symbols

Physical Constants

α_s	The strength of the strong interaction
$\hbar$	The reduced Planck's constant. $\hbar = \frac{h}{2\pi} \approx 1.0546 \times 10^{-34}$ J s
c	The speed of light in vacuum $299,792,458$ m/s
g_{QCD}	The QCD coupling constant

Mathematical symbols

$:=$	A definition
$[A, B]$	The commutator of A and B
δ_μ^ν	The Kronecker delta
$\mathbb{A}^T$	The transpose of a matrix $\mathbb{A}$
$\mathbb{A}^{-1}$	The inverse of a matrix $\mathbb{A}$
$\mathbb{C}$	The set of complex numbers
$\mathbb{C}^{n,m}$	The space of complex $n \times m$ matrices
$\mathbb{N}$	The set of natural numbers
$\mathbb{R}$	The set of real numbers
$\mathrm{diag}\,(x_1, x_2, ..., x_n)$	A diagonal matrix with the values $x_1, x_2, ..., x_n$ on its diagonal
$\mathrm{rank}(\mathbb{A})$	The rank of the matrix $\mathbb{A}$
$\mathrm{Tr}(\mathbb{A})$	The trace of the matrix $\mathbb{A}$
$\overline{A}$	The complex conjugate of A
$\not{X}$	The Feynman slash notation
$E[x]$	The expectation value of x
f^{abc}	The structure constants
i	The imaginary unit
$N(\mu, \sigma)$	The normal distribution with mean μ and standard deviation σ

Other Symbols

e.g.	*(exempli gratia)* For example
etc.	*(et cetera)* And other things

Physical quantities

η	The pseudorapidity
$\mathscr{L}$	The Lagrangian density
μ, ν	4-vector indices
ϕ	The azimuthal angle
ψ	The bispinor
a, b, c	Colour indices
A_μ^a	The vector (gauge) potential
D_μ	The covariant derivative
$F_{\mu\nu}$	The electromagnetic field tensor
$g_{\mu\nu}$	The metric tensor
$G_{\mu\nu}^a$	The gluon field strength tensor
J	The angular momentum
m	Mass
p_{T}	The transverse momentum
Q	The four-momentum transfer of a collision
y	The rapidity

Introduction

Scattering experiments played an integral part in nuclear and sub-nuclear physics. They help in the study of the structure of matter and historically yielded several fundamental discoveries. For example the discovery of the atomic nucleus by E. Rutherford [1] and the discovery of the non-point-like character of the proton by R. Hofstadter [2]. Furthermore, scattering experiments [3–5] of electrons on protons at SLAC in the 60s revealed a rich inner structure of the proton and helped in the development of the quark model for which three physicists—Jerome I. Friedman, Henry W. Kendall and Richard E. Taylor—won the 1990 Nobel Prize. A significant milestone in the understanding of hadrons was the discovery of Quantum Chromodynamics [6, 7] and its subsequent integration with the parton model.

In scattering experiments, it is important that the de Broglie wavelength of particles shortens as their momentum increases which allows to get better spatial resolution. The Large Hadron Collider at CERN, at present the largest particle accelerator in the world, therefore allows to study the structure of the proton in a kinematic region which has never been explored so far. Hard processes between interacting partons can reveal interesting information about the proton at small Bjorken x values. In the final state of a hard scattering where quarks and gluons are involved one can usually find a collimated shower of high energy particles the so-called jet. In principle, by assigning the particles to a jet one can gain more information about the outgoing parton. The assignment of particles to jets is often ambiguous because it is not clear whether a particle belongs to a jet or not. Therefore many jet algorithms have been developed and nowadays they provide a consistent connection between the theoretical and experimental results. Apart from the useful information that jets convey about the inner structure of the proton, jets also serve as an efficient tool in the study of the Quark Gluon Plasma (QGP) [8, 9]. Understanding jet production in elementary processes is thus crucial for these measurements.

The aims of this thesis are:

- to get familiar with QCD, hard processes, fragmentation and jets,
- to describe the ALICE experiment,
- to analyse measured, uncorrected jet spectra from p + p collisions at $\sqrt{s} = 13$ TeV based on runs that passed a quality assessment,
- to corrected the measured spectra for detector effects,
- to estimate systematic errors of the data,
- to compare the results with Monte Carlo generators.

Chapter 1

Hard scattering processes in p+p

During relativistic proton-proton $(\mathrm{p}+\mathrm{p})$ collisions at the LHC, the interaction usually takes place on the level of fundamental constituents—quarks and gluons. The description of this interaction is provided by Quantum Chromodynamics.

Quantum Chromodynamics (QCD) [10] is the accepted fundamental theory of the strong interaction describing the interaction between particles possessing the colour charge, quarks and gluons. QCD is a non-abelian quantum field theory invariant under local $SU(3)_c$ gauge transformations.

The basic concepts of QCD shall be outlined in the subsequent chapters and the following conventions shall be used in this chapter. The units are fixed such that the speed of light and the reduced Planck's constant are $c = 1$, $\hbar = 1$. Greek indices $(\mu, \nu, \cdots)$ denote elements of a 4-vector. Latin indices $(a, b, \cdots)$ are used to denote colour degrees of freedom unless explicitly stated otherwise. A repeated index invokes the Einstein summation rule where an implicit summation is taken over the repeated index. Furthermore, the Feynman slash rule is used $\not{A} := \gamma^\mu A_\mu$ where $\gamma^0, \gamma^1, \gamma^2, \gamma^3$ are Dirac matrices.

1.1 Cross-sections

At present it is impossible to compute cross-sections of a hard interaction of composite objects like protons or neutrons solely from basic principles. A cross-section of an interaction such as $p+p \to h+X$, where X stands for all possible final states has to be calculated phenomenologically [11]. The interaction of a composite object is decomposed into three temporally distinct phases. The initial internal structure of the incoming composite particles before the collision is encompassed in the *parton distribution functions* which describe the distribution of quarks and gluons inside the proton long before the interaction occurs. Then an elementary interaction which is calculable from QCD takes place. The elementary process is of short duration and does not affect a *hadronisation* phase that occurs long after the interaction. This factorisation is summarised as

$$\sigma_{A+B\to h+X} = \sum_{a,b,c,d} \int dx_1\, dx_2\, f_{a/A} \cdot f_{b/B} \cdot \sigma_{a+b\to c+d} * D_{h/c}, \tag{1.1}$$

where $\sigma_{A+B\to h+X}$ is the cross section of the interaction of two composite objects A and B containing partons a and b respectively, $f_{i/I}(x, Q^2)$ are parton distribution functions of the parton i in the composite object I dependent on the fraction of the momentum carried by the parton x and the energy scale Q^2, $\sigma_{a+b\to c+d}$ is the elementary cross section of partons $a+b \to c+d$

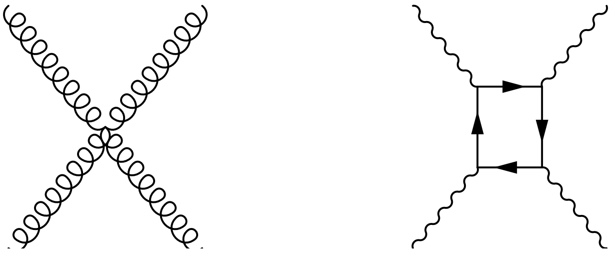

Figure 1.1: **Left**: Gluon self interaction in QCD is allowed in the lowest perturbative order. **Right**: Lowest order diagram of $\gamma\gamma$ scattering. The scattering is enabled by means of a fermion loop.

and $D_{h/c}(z, p_{\mathrm{T}})$ is the fragmentation function of parton c that yields the hadron h carrying the fraction z of the original parton energy and the transverse momentum p_{T}. The sum over all combination of partons a, b, c and d is taken and $*$ signifies further integration over the momenta p_c and p_d that lead to the final state [11]. All of these terms shall be examined further.

1.2 The QCD Lagrangian

The Lagrangian density of QCD [10] is

$$\mathcal{L}_{QCD} = \sum_{\text{flavour}} \overline{\psi} \left(i\not{D} - m \right) \psi - \frac{1}{4} G^a_{\mu\nu} G_a^{\mu\nu}, \tag{1.2}$$

where ψ is a 4-component Dirac spinor describing a quark field, $D_\mu = \partial_\mu - i g_{QCD} A^a_\mu T_a$ is the covariant derivative of QCD, $\overline{\psi} := \psi^\dagger \gamma^0$ is the Dirac conjugate of ψ, $G^a_{\mu\nu} := \partial_\mu A^a_\nu - \partial_\nu A^a_\mu + g_{QCD} f^{abc} A^b_\mu A^c_\nu$ is the gluon field strength tensor, g_{QCD} is the coupling constant of the strong interaction and T_a are the generators of the colour $SU(3)$ group under which the local gauge transformation $\psi \rightarrow e^{-i\alpha(x)^a T_a}\psi$, $a \in \{1, \ldots, 8\}$ holds while the gluon field A^a_μ also transforms.

The peculiar nature of QCD is well demonstrated by a comparison with Quantum Electrodynamics (QED). For this purpose, consider the QED Lagrangian density [10]

$$\mathcal{L}_{QED} = \overline{\psi} \left(i\not{D} - m \right) \psi - \frac{1}{4} F_{\mu\nu} F^{\mu\nu}, \tag{1.3}$$

where $F_{\mu\nu}$ is the electromagnetic field strength tensor defined as $F_{\mu\nu} = \partial_\mu A_\nu - \partial_\nu A_\mu$ and A_μ is the electromagnetic 4-potential, i.e. the photon field. Analogously to QED, the gluon field strength tensor $G^a_{\mu\nu}$ describes the dynamics of the gluon field A^a_μ. However, it has an extra term. Since gluons carry colour degrees of freedom, in contrast to photons which do not possess the electromagnetic charge, the term $g_{QCD} f^{abc} A^b_\mu A^c_\nu$ results in gluon self interactions. Thus interactions of the kind seen in Fig. 1.1 (Left) are physically allowed, whereas photon self interactions are not allowed in the leading order of QED. In higher orders of perturbation photons can e.g. interact via a fermion loop shown in Fig. 1.1 (Right).

1.3 Elementary QCD cross-sections

Using the QCD Lagrangian (1.2) one can calculate various elementary cross-sections σ which enter (1.1). For example, Table 1.1 presents spin averaged, leading order invariant amplitudes

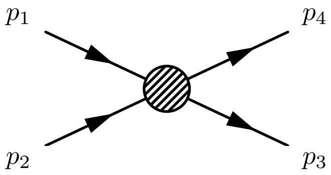

Figure 1.2: The scheme of a particle interaction. 4-momenta of incoming particles are denoted p_1 and p_2, 4-momenta of outgoing particles are labelled as p_3 and p_4.

for basic $2 \to 2$ processes of unpolarised quarks, antiquarks and gluons. Quarks and antiquarks are assumed massless. Here s, t, u denote Mandelstam variables which are defined as

$$s = (p_1 + p_2)^2\,, \tag{1.4}$$

$$t = (p_1 - p_4)^2\,, \tag{1.5}$$

$$u = (p_1 - p_3)^2\,, \tag{1.6}$$

where p_1, p_2, p_3 and p_4 are 4-momenta of particles involved in the $2 \to 2$ interaction defined in Fig. 1.2.

Process	$\frac{\lvert\overline{\mathcal{M}}\rvert^2}{g^4}$
$qq' \to qq'$ $\overline{q}q' \to \overline{q}q'$	$\frac{4}{9}\frac{s^2+u^2}{t^2}$
$qq \to qq$	$\frac{4}{9}\left(\frac{s^2+u^2}{t^2} + \frac{s^2+t^2}{u^2}\right) - \frac{8}{27}\frac{s^2}{ut}$
$\overline{q}q \to \overline{q}'q'$	$\frac{t^2+u^2}{s^2}$
$\overline{q}q \to \overline{q}q$	$\frac{4}{9}\left(\frac{s^2+u^2}{t^2} + \frac{t^2+u^2}{s^2}\right) - \frac{8}{27}\frac{u^2}{st}$
$\overline{q}q \to gg$	$\frac{32}{27}\frac{u^2+t^2}{ut} - \frac{8}{3}\frac{u^2+t^2}{s^2}$
$gg \to \overline{q}q$	$\frac{1}{6}\frac{u^2+t^2}{ut} - \frac{8}{3}\frac{u^2+t^2}{s^2}$
$qg \to qg$	$-\frac{4}{9}\frac{u^2+s^2}{ut} + \frac{u^2+s^2}{t^2}$
$gg \to gg$	$\frac{9}{2}\left(3 - \frac{ut}{s^2} - \frac{us}{t^2} - \frac{st}{u^2}\right)$

Table 1.1: Elementary QCD cross sections of different $2 \to 2$ processes at the leading order [12].

The angular distribution can be obtained from the Mandelstam variables u and t as

$$t = -\frac{1}{2}s\,(1 - \cos\theta)\,, \tag{1.7}$$

$$u = -\frac{1}{2}s\,(1 + \cos\theta)\,, \tag{1.8}$$

where θ is the scattering angle in the centre-of-mass system. The elementary invariant amplitudes as functions of $\cos\theta$ are plotted in Figure 1.3. The mid-rapidity region[1] is located around $\cos\theta = 0$. Note that for some processes the forward-backward asymmetry is apparent, e.g. $\overline{q} + q \to \overline{q} + q$.

---

[1] The central barrel of the ALICE experiment covers the pseudorapidity range $|\eta| < 0.9$, which corresponds to an approximate scattering angle interval $\theta \in (44^\circ, 136^\circ)$ or $\cos\theta \in (-0.7, 0.7)$.

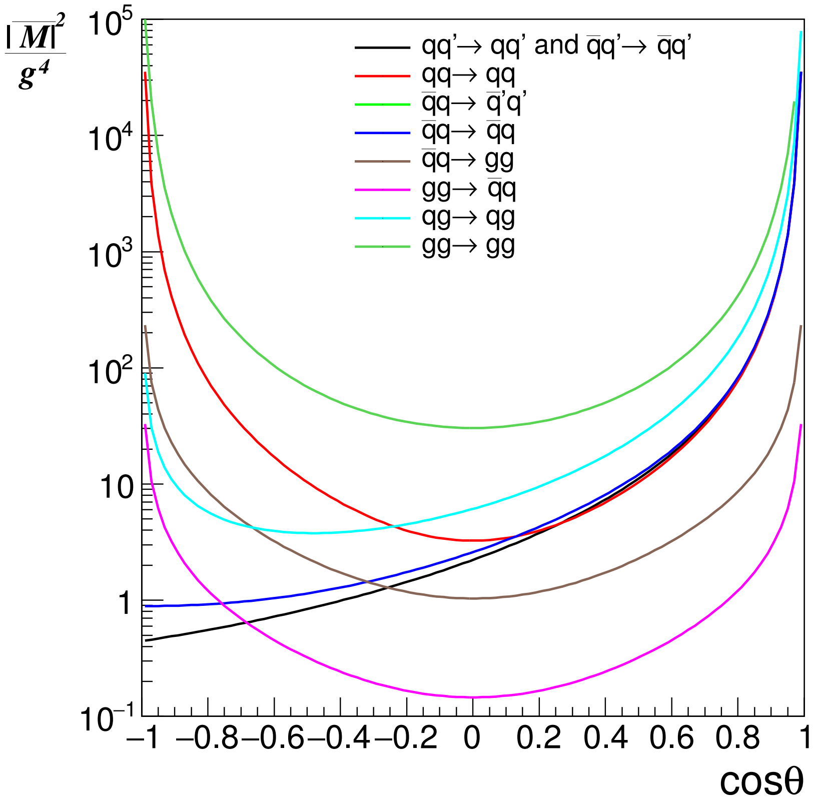

Figure 1.3: $\frac{|\overline{\mathcal{M}}|^2}{g^4}$ plotted for different 2 body processes as given in Table 1.1.

1.4 Asymptotic freedom

The size of the coupling in QCD, $g_{QCD} = \sqrt{4\pi\alpha_S}$ depends on the transferred 4-momentum. For large momentum transfers the QCD coupling decreases to zero—a phenomenon known as *asymptotic freedom* [13]. For small momentum transfers the coupling diverges. This behaviour of the coupling can be explained as follows. In QED, free charges are surrounded by a cloud of virtual fermion anti-fermion pairs arising from vacuum. This is known as vacuum polarisation and is responsible for the screening of the electric charge [11]. This leads to a notion of an effective charge—the net charge of the particle and its surrounding cloud of particle anti-particle pairs.

The screening effect is also present in QCD. However, the fact that gluons posses colour degrees of freedom introduces a new phenomenon—anti-screening. Virtual gluons can be created from vacuum and enhance the net colour charge and therefore affect the coupling strength. The change in the coupling strength due to screening effects is known as the running of the coupling constant [11].

One can quantify the running of the coupling constant by the β-function which is derived from the renormalisation group [13], [14]. The derivation shall be carried out in the subsequent text. Consider a dimensionless observable $F(Q^2)$ dependent on the energy scale Q^2. Renormalisation introduces a new energy scale μ. Since the observable $F(Q^2)$ only depends on one parameter, defining $\alpha_s \equiv F(\mu^2)$ as a measurable renormalised coupling constant will fully determine the renormalised theory.

The renormalisation of the perturbative expansion of $F(Q^2)$ must not depend on the renormalisation scale μ meaning that fixing a different value of ${\alpha_s}' \equiv F({\mu'}^2)$ must yield the same renormalisation of $F(Q^2)$. This independence of the renormalisation procedure on the renormalisation scale is called the group condition. Since there is no explicit mass scale in the QCD Lagrangian, in order for $F(Q^2)$ to be dimensionless, it must be a function of the ratio Q^2/μ^2 [13].

The introduction of a renormalisation scale μ and the group condition leads to a differential equation for μ

$$\mu^2 \frac{\mathrm{d}}{\mathrm{d}\mu^2} F\left(\frac{Q^2}{\mu^2}\right) = 0 \Leftrightarrow \left[\mu^2 \frac{\partial}{\partial \mu^2} + \mu^2 \frac{\partial \alpha_S}{\partial \mu^2} \frac{\partial}{\partial \alpha_s}\right] F\left(\frac{Q^2}{\mu^2}\right) = 0. \tag{1.9}$$

Introducing $\tau = \ln\left(\frac{Q^2}{\mu^2}\right)$ and $\beta(\alpha_s) = \mu^2 \frac{\partial \alpha_S}{\partial \mu^2}$ gives

$$\left[-\frac{\partial}{\partial \tau} + \beta(\alpha_S) \frac{\partial}{\partial(\alpha_S)}\right] F\left(\frac{Q^2}{\mu^2}\right) = 0. \tag{1.10}$$

Solving the differential (1.10) yields an expression for $\beta(\alpha_S)$. Consider

$$\frac{\partial F}{\partial \tau} = \beta\left(\alpha_s\right) \frac{\partial F}{\partial \alpha_S} \Leftrightarrow \frac{1}{\beta\left(\alpha_S\right)} \frac{\partial \alpha_S}{\partial F} = \frac{\partial \tau}{\partial F}, \tag{1.11}$$

multiplying the last equation by the Jacobian $\frac{\partial F}{\partial \alpha_S}$ gives

$$\frac{1}{\beta\left(\alpha_S\right)} = \frac{\partial \tau}{\partial \alpha_S} \Leftrightarrow \int_0^{\alpha_S(Q^2)} \mathrm{d}\tilde{\alpha}_S \frac{1}{\beta\left(\tilde{\alpha}_S\right)} + C = \int_0^{\alpha_S(Q^2)} \mathrm{d}\tilde{\alpha}_S \frac{\partial \tau}{\partial \tilde{\alpha}_S} = \tau. \tag{1.12}$$

Equation (1.10) has no initial or boundary conditions and therefore has a class of functions as its solution (signified by an arbitrary constant C). A concrete solution is chosen from the class by fixing C. In this case, it is convenient to shift the lower limit of integration to a known value by picking $C \equiv \int_{\alpha_S(\mu^2)}^0 \mathrm{d}\tilde{\alpha}_S \frac{1}{\beta(\tilde{\alpha}_S)}$. The chosen solution to equation (1.10) is thus expressed as a function of the upper limit of the integral

$$\tau = \ln\left(\frac{Q^2}{\mu^2}\right) = \int_{\alpha_S(\mu^2)}^{\alpha_S(Q^2)} \mathrm{d}\tilde{\alpha}_S \frac{1}{\beta\left(\tilde{\alpha}_S\right)}. \tag{1.13}$$

The β-function can now be expressed perturbatively in powers of α_S as

$$\beta(\alpha_S) = \sum_{n=0}^{+\infty} \beta_n \alpha_S^n, \tag{1.14}$$

where $\beta_0 = \beta_1 = 0$. At a one-loop order the equation becomes

$$\beta_2 \ln\left(\frac{Q^2}{\mu^2}\right) = \int_{\alpha_S(\mu^2)}^{\alpha_S(Q^2)} \mathrm{d}\tilde{\alpha}_S \frac{1}{\tilde{\alpha}_S^2(Q)} = \frac{1}{\alpha_S(\mu^2)} - \frac{1}{\alpha_S(Q^2)}, \tag{1.15}$$

and thus

$$\alpha_S(Q^2) = \frac{\alpha_S(\mu^2)}{1 - \beta_2 \alpha_S(\mu^2) \ln\left(\frac{Q^2}{\mu^2}\right)}. \tag{1.16}$$

For the one-loop expansion in QED $\beta_2 = \frac{1}{3\pi}$ and in QCD $\beta_2 = -\frac{11N_c - 2N_f}{12\pi} = -\frac{7}{4\pi}$, where $N_c = 3$ is the number of colours and $N_f = 6$ is the number of flavours. In QED, β_2 is positive and

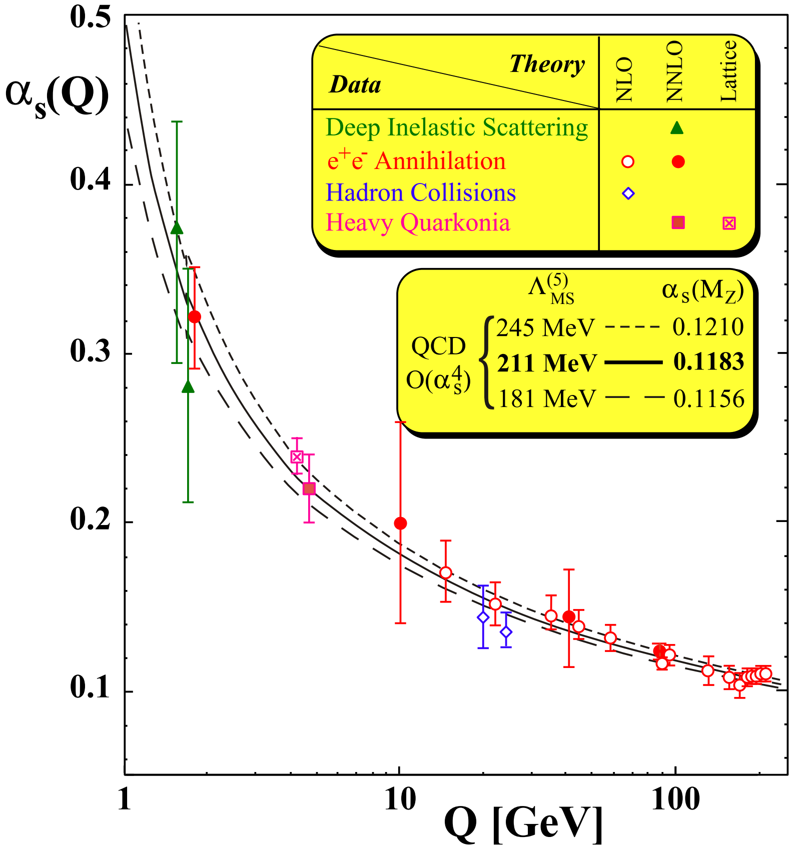

Figure 1.4: Measurement of the running of the strong coupling constant α_s. The solid line is a theoretical prediction. Points represent experimentally determined values. The point with the square marker with an "X" has been obtained from non-perturbative lattice QCD. Taken from [15].

thus the coupling increases with larger Q^2. On the other hand in QCD β_2 is negative and the coupling decreases with increasing Q^2.

Equation (1.16) describes the running of the coupling constant with Q^2. The fact that

$$\lim_{Q^2 \to \infty} \alpha_S(Q^2) = 0, \tag{1.17}$$

represents *asymptotic freedom*— the higher the energy (shorter probe wavelength) the weaker the strong coupling appears to be. The behaviour of α_S can be seen in Figure 1.4.

1.5 Parton distribution functions

A parton distribution function $f_{i/I}(x, Q^2)$ gives the probability distribution of finding a parton with flavour i in the given hadron carrying a fraction x of the total hadron momentum having the squared 4-momentum transfer of the hard interaction Q^2 [16]. Parton distribution functions are measured using deep inelastic scattering of leptons on nucleons [11]. The presumption that electrons and neutrinos have no internal structure is utilised. The current knowledge of the parton distribution functions of a proton is shown in Figure 1.5. The plot shows separately the distribution of valence quarks u and d and the distribution of gluons (labelled g) and sea quarks

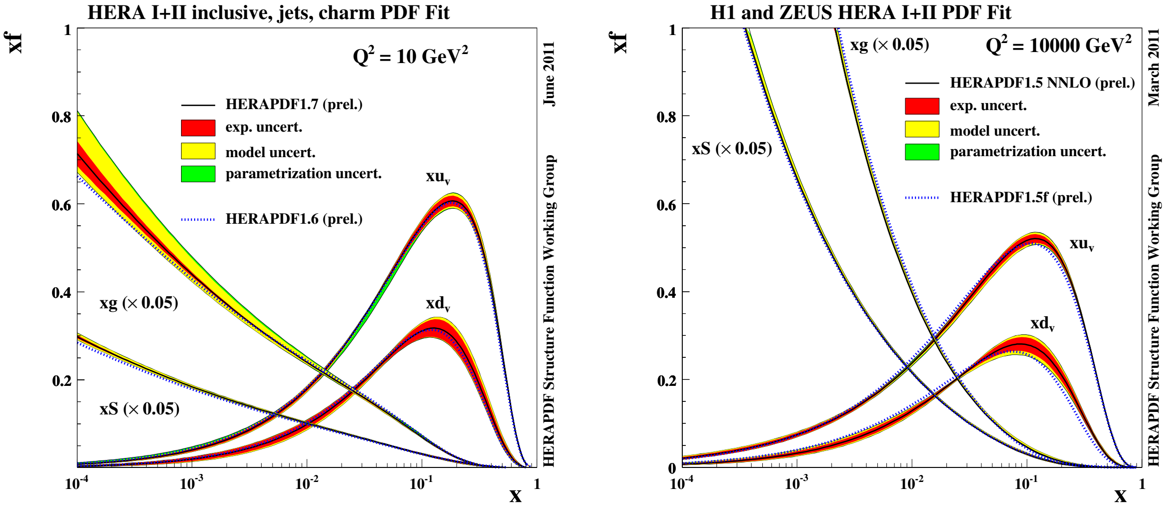

Figure 1.5: The (proton) parton distribution functions from HERAPDF1.7 at $Q^2 = 10$ GeV^2 **Left** and $Q^2 = 10000$ GeV^2 **Right**. The gluon and sea distributions are scaled down by a factor 20. The experimental, model and parametrisation uncertainties are shown separately. For comparison, the central values of HERAPDF1.6 are also shown [16].

(labelled as S). Note, that the parton distribution functions are plotted scaled by x. At large x, parton distribution functions are dominated by valence quarks.

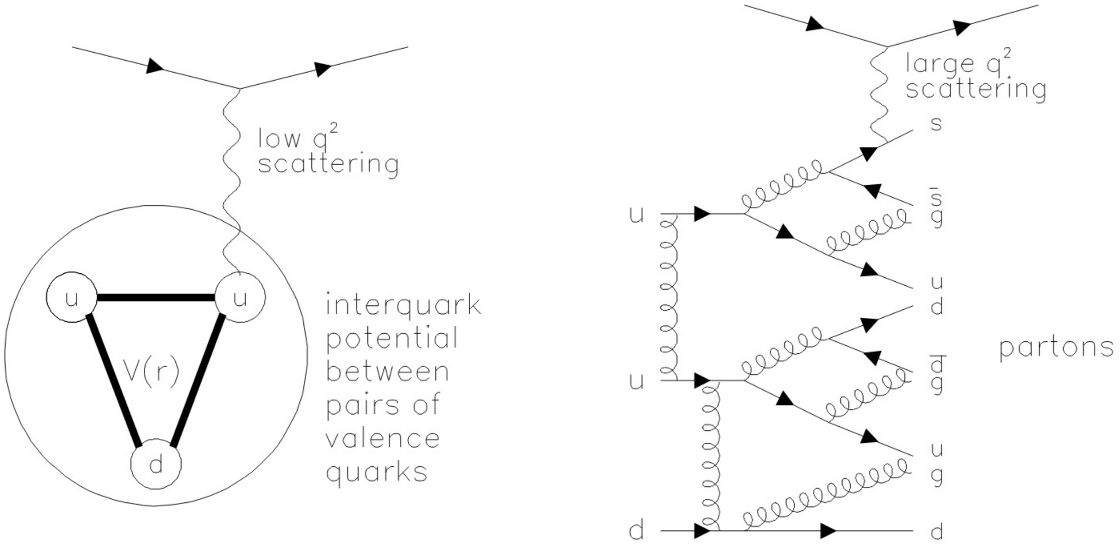
low q^2 scattering
u
u
d
V(r)
interquark potential between pairs of valence quarks
large q^2 scattering
s
$\bar{s}$
g
u
d
d
$\bar{d}$
g
u
g
d
u
u
d
partons

Figure 1.6: The proton structure as probed at different Q^2. **Left:** A lepton scattering on a proton at low Q^2. **Right:** A lepton scattering on a proton at high Q^2. Taken from [11].

The proton picture is dependent on the wavelength by which it is observed. When a proton is observed at low resolution, for example with a low Q^2 electron scattering, it behaves as three valence quarks bound by a static potential as depicted in the left part of Figure 1.6. On the other

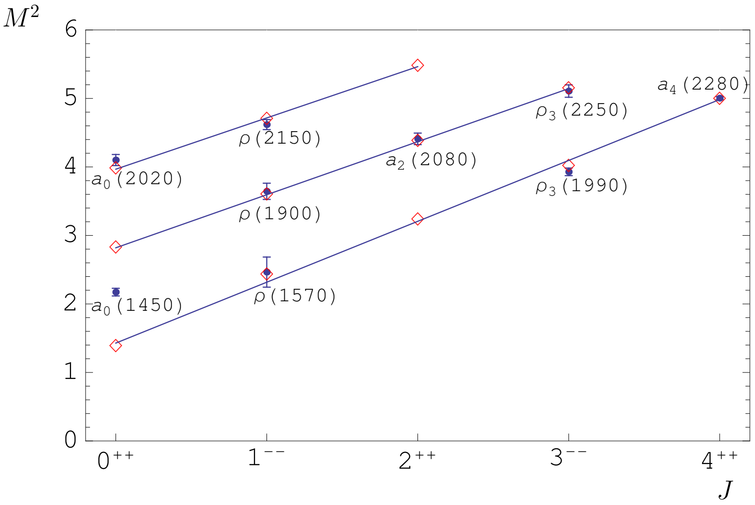

Figure 1.7: Parent and daughter (J, M^2) Regge trajectories for isovector light mesons with natural parity (ρ). Diamonds are predicted masses. Available experimental data are given by dots with error bars and particle names. M^2 is in GeV^2 [17].

hand, a hard process can distinguish a virtual particle—anti-particle pair that has been created from a gluon. The sea quarks are all virtual particles and must annihilate in a short amount of time given by the Heisenberg uncertainty relations. If the Q^2 is high the probe (lepton) will most likely scatter on a virtual particle (see Figure 1.6 right) [11]. The proton is therefore dominated by sea quarks at high resolutions.

The proton-proton collisions at $\sqrt{s} = 200$ GeV which are measured at RHIC are therefore dominated by $q + q$ processes whereas the LHC accelerates protons to $\sqrt{s} = 13$ TeV and is dominated by $g + g$ processes [12].

1.6 Confinement

Fragmentation functions give the probability that after an interaction the quark q forms the hadron h with transverse momentum p_{T} and carries the fraction z of its energy. Thus these functions phenomenologically describe the probability of the transition of an object with colour charge to a colour-neutral state and reflect *colour charge confinement* [11].

The colour charge confinement is a feature of QCD postulating that no colour charge can exist in an isolated state. Although the detailed quantitative understanding of colour confinement is still an open question, it is supported by the extensive lack of observations of any isolated colour charges.

Historically various phenomenological models that describe confinement of quarks in hadrons have been developed. The MIT Bag model [18] is used to describe quarks in stationary (non-perturbative regime of QCD) hadrons. It assumes that the quarks are massless objects in a bag. Confinement arises with the introduction of the inward bag pressure B which is balanced by the kinetic energy of the quarks inside the bag. It can be shown [18] that the bag pressure is related to the number of particles in the bag N and the size of the bag R as

$$B^{\frac{1}{4}} = \left(\frac{2.04N}{4\pi}\right)^{\frac{1}{4}} \frac{1}{R}. \tag{1.18}$$

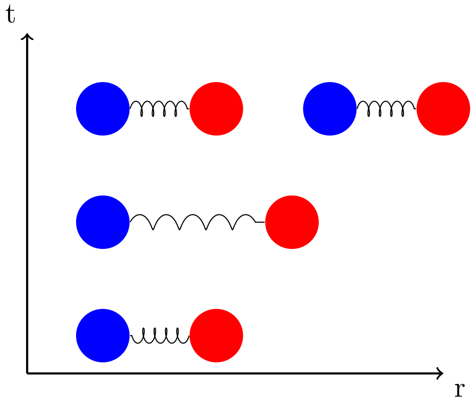

Figure 1.8: QCD colour confinement in the string model. Two quarks with a string are pulled apart. The potential energy in the string increases until a pair of virtual particles is created from vacuum which restores the colour neutrality of the original object.

The confinement radius for a 3 quark system can be taken as $R = 0.8$ fm to yield the value of the bag pressure $B^{\frac{1}{4}} = 206$ MeV, which is consistent with the experimental limits 145 MeV $< B^{\frac{1}{4}} <$ 235 MeV [18].

A simple Bag model however, is not suitable for the description of the dynamics of the colour confinement in hadronisation. A more suitable model [18] envisions the field between quarks as a colour string. The gluon self-interaction restricts the colour field into strings between individual quarks in a hadron. To model the colour string between quarks, the effective QCD potential can be introduced in the form

$$V^{\text{eff}}_{QCD} = -\frac{4}{3}\frac{\alpha_S}{r} + kr, \tag{1.19}$$

where r is the distance and $k \sim 1$ GeV/fm is the string tension. This potential is obtained from excited states of quarkonia and is supported by the existence of Regge trajectories in hadron spectra. Regge trajectories are experimentally observed dependencies of square mass M^2 and spin J of hadron resonances. Hadron resonances with identical internal symmetry quantum numbers but different spins lie on a trend where M^2 is a linear function of J [18], see Figure 1.7 which shows the Regge trajectories for ρ mesons. Confinement in the perturbative regime is modelled using this linear string potential kr.

Consider a particle—anti-particle pair connected by a colour string. The pair of bound particles oscillates in a so-called yo-yo mode. When trying to separate these two bound quarks by transferring energy to them, the potential energy in the hypothetical string grows with increasing distance until it prompts the creation of a particle—anti-particle pair from vacuum as depicted in Figure 1.8. Thus two strings are formed which leads to the production of hadrons and the restoration of the colour neutrality of the $q\bar{q}$ giving rise to the confinement of the colour charge.

The Lund model [12] gives the probability distribution of the locations of the vertices at which the string is broken. The vertices lie approximately on the constant proper time world line [18]. The worldlines of the interacting particles and the subsequent breaking of the string into new particles with their worldlines are illustrated in Figure 1.9.

Thus when two partons interact via a hard process the phenomenon of confinement leads to the production of new particles—*fragmentation*. It is the result of the restoration of the colour neutrality of the interacting partons. Therefore hard processes with quarks and gluons in the

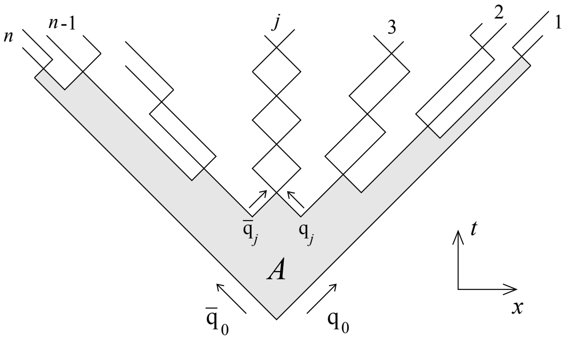

Figure 1.9: The break-up in space–time of a Lund colour string into n hadrons. The fragmentation area is denoted by A [19]. The rectangles correspond to yo-yo modes of quark strings in the produced hadrons. The area of a closed yo-yo cycle corresponds to the produced particle's mass.

final state are characteristic by the production of showers of particles in the form of jets. Gluons carry more colour charge then quarks and therefore generally fragment to more particles than quarks [10].

Fragmentation remains poorly understood from the first principles of QCD and the use of phenomenological models such as the Lund model is needed in order to simulate the final state of hard interactions. The Lund model is implemented in the widely used Monte Carlo generator PYTHIA [20].

1.7 Jets

A phenomenon that arises with hard scattering processes with a quark or a gluon in the final state is the formation of collimated high energy particle showers that originated in parton showering and a subsequent hadronisation. These showers are called *jets*. The hadronisation phase obscures the information about the initial hard scattering process. Historically the determination of the 4-momentum of the hadron shower has been attempted in order to reconstruct the kinematics of outgoing scattered partons. This however cannot be done unambiguously and the concept of a phenomenological jet has been introduced. While jets have a theoretical foothold in QCD only a phenomenological definition is utilised henceforth.

A jet is defined by an heuristic algorithm—the jet algorithm that clusters individual final state hadrons. The jet algorithm reassembles the 4-momenta of all the final state hadrons in the shower and thereby extracts information about the original parton that led to the formation of the jet. The two algorithms that are further utilised are the k_T and anti-k_T algorithms.

- **The k_T algorithm** is a sequential recombination algorithm [21]. The following metrics are used in the k_T algorithm for hadron collisions when grouping particles into a jet

$$d_{ij} = \min(p_{\mathrm{T},i}^2, p_{\mathrm{T},j}^2)\frac{\Delta R_{ij}^2}{R^2}, \qquad \Delta R_{ij}^2 = (y_i - y_j)^2 + (\phi_i - \phi_j)^2\,, \tag{1.20a}$$

$$d_{iB} = p_{\mathrm{T},i}^2, \tag{1.20b}$$

  where p_T, y and ϕ are the transverse momentum, rapidity and the azimuthal angle respectively. The first metric (1.20a) is a metric concerning two particles i and j whereas metric (1.20b) is a metric between particle i and the beam. The k_T algorithm first computes all the metrics then if d_{ij} is smaller than d_{iB} particles i and j are combined into a pseudojet and the metrics are calculated again. Note that the term particle is used for both real particles and pseudojets alike. If d_{iB} is smaller than every d_{ij} it declares the pseudojet i as a jet and removes it from the set of particles and the metrics are computed again. This procedure is iterated until no particles remain in the set. Note that the concept of a pseudojet is a purely algorithmic construct and can be thought of as a collection of particles. The k_{T} algorithm starts the clusterisation of particles with the softest ones.

- **The anti-k_{T} algorithm** follows [21] an identical procedure as the k_{T} algorithm only the metric is changed to

$$d_{ij} = \min(p_{\mathrm{T},i}^{-2}, p_{\mathrm{T},j}^{-2})\frac{\Delta R_{ij}^2}{R^2}, \qquad \Delta R_{ij}^2 = (y_i - y_j)^2 + (\phi_i - \phi_j)^2\,, \tag{1.21a}$$

$$d_{iB} = p_{\mathrm{T},i}^{-2}. \tag{1.21b}$$

In the case of the anti-k_{T} algorithm, the jets are built starting with particles with the highest p_{T} .

Both the k_{T} and the anti-k_{T} algorithms satisfy the essential conditions on a jet algorithm namely infrared (IR) and collinear safety which are essential for the correspondence between phenomenological jets and QCD jets. *Infrared safety* means that the radiation of an IR gluon must not change the particle configuration of jets. *Collinear safety* means that the collinear splitting of particles must not change the configuration of jets. IR and collinear safety are illustrated in Figures 1.10 and 1.11 respectively.

The necessity of these conditions is illustrated by the spectrum of gluons emitted in a $q \to qg$ process. The differential spectrum in the leading order is given by [22]

$$\mathrm{d}w^{q\to qg} = \frac{2\alpha_S(k_{\mathrm{T}}^2)}{3\pi}\left[1 + \left(1 - \frac{k}{E}\right)^2\right]\frac{\mathrm{d}k}{k}\frac{\mathrm{d}k_{\mathrm{T}}^2}{k_{\mathrm{T}}^2}, \tag{1.22}$$

where k^μ is the 4-momentum of the radiated gluon, E is its energy, k its longitudinal momentum and k_{T} its transverse momentum. This spectrum exhibits an infrared divergence at $k \to 0$ and a collinear divergence at $k_{\mathrm{T}} \to 0$. The emitted gluons would therefore mostly have a small energy and would be emitted in the forward direction meaning that the emitted gluons would be preferentially collinear and soft. However, in the next-to-leading order these divergences cancel with the contribution from loop diagrams and the cross section remains finite. This is due to the Kinoshita-Lee-Nauenberg/Block-Nordsieck theorem [23] which states that soft and collinear divergences cancel between real and virtual diagrams at any given order of the perturbation theory.

To get a consistent relation between observables in the theory and experiment this cancellation must be preserved and therefore the observable has to be insensitive to collinear branchings and soft emissions. Therefore the jet reconstruction algorithms have to be infrared and collinear safe in order to yield finite cross sections.

Both the k_{T} and the anti-k_{T} algorithm are implemented in the *FastJet* package [24]. One of the differences between the k_{T} and the anti-k_{T} algorithms lies in the shapes of the jet. *FastJet* determines the shape of the jet area by an addition of very soft particles called *ghost particles* which are discussed in the following chapter. The anti-k_{T} algorithm produces more rounded jets than the k_{T} algorithm. This is shown in Figure 1.12. Furthermore, the k_{T} algorithm prefers to cluster low p_{T} particles first as opposed to the anti-k_{T} algorithm which is apparent from

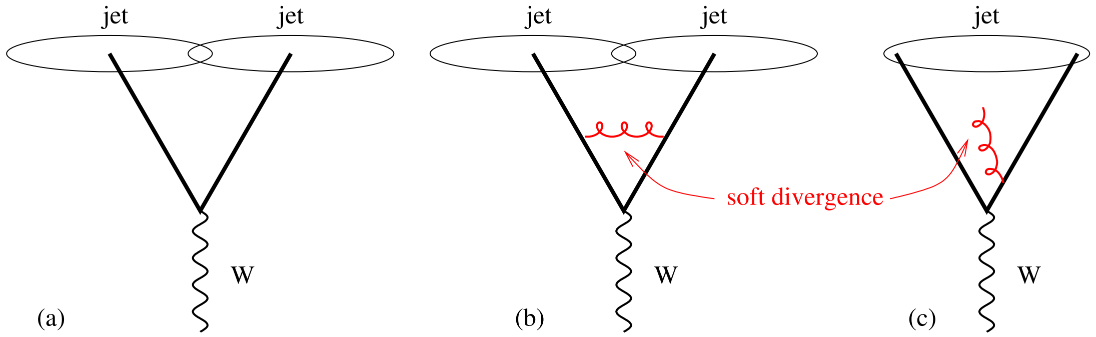
jet
jet
jet
jet
jet
soft divergence
W
W
W
(a)
(b)
(c)

Figure 1.10: Infrared unsafety of jet algorithms. Picture a) shows the initial definition of jets. The emission of a soft gluon in picture c) has converted the event from having two jets to just one jet whereas the emission of a soft gluon in picture b) did not change the configuration of jets [21].

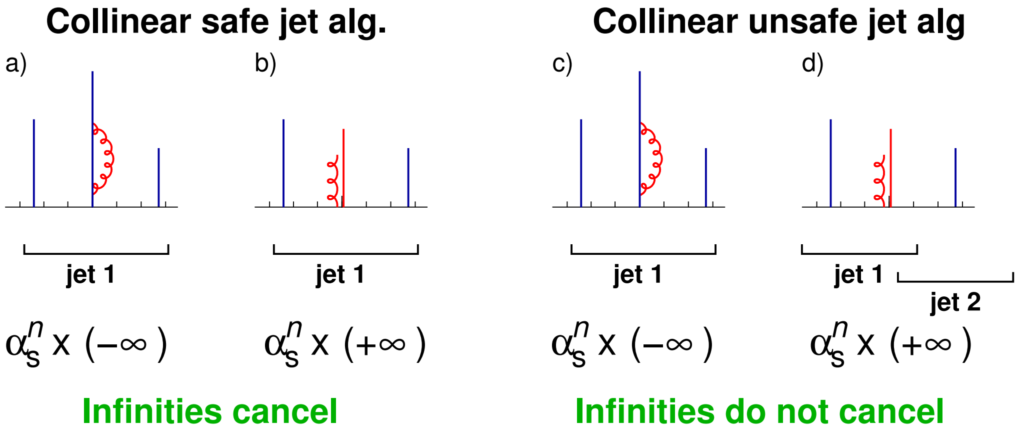
Collinear safe jet alg.
Collinear unsafe jet alg
a)
b)
c)
d)
jet 1
jet 1
jet 1
jet 1
jet 2
α_s^n x (−∞)
α_s^n x (+∞)
α_s^n x (−∞)
α_s^n x (+∞)
Infinities cancel
Infinities do not cancel

Figure 1.11: Collinear safety of jet algorithms. Pictures a) and b) illustrate collinearly safe algorithms where the emission of a collinear gluon does not change the definition of a jet whereas pictures c) and d) illustrate collinearly unsafe algorithms [21].

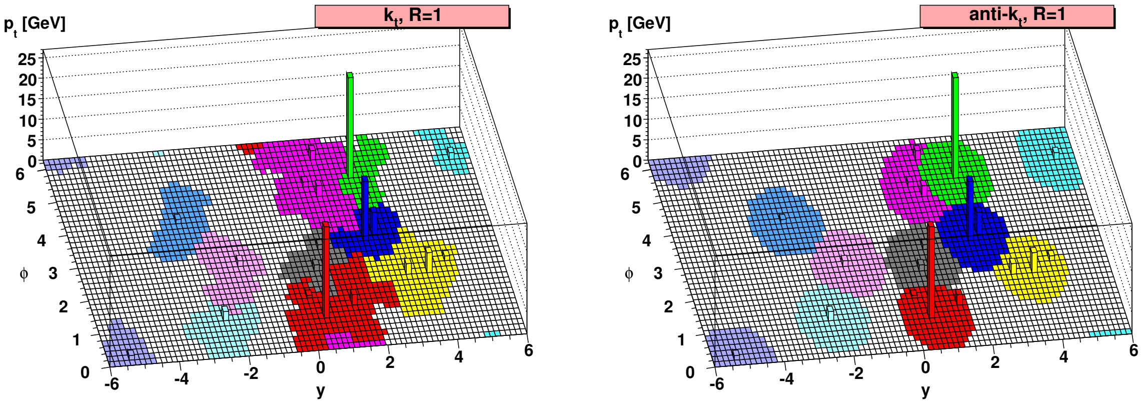

Figure 1.12: The comparison of the rapidity-azimuthal distributions of jets for the **Left**: k_{T} and the **Right**: anti-k_{T} algorithms [21].

their metrics definitions (1.20) and (1.21). This is used in jet analyses of heavy-ion collisions where it is difficult to distinguish a jet from a soft background. In this case, it is convenient to start building jets from the hardest particles because hard particles could have originated only in a hard scattering. On the other hand, the background is dominated by soft particles whose density is estimated by the k_{T} algorithm [25].

1.8 Background subtraction

Jets originate from hard parton-parton scatterings in particle collisions. The products of a hard scattering is accompanied by the so called underlying event [26] which encompasses particles produced by other processes during the collision and which are believed to be uncorrelated with the hard scattering process. An example of such a process is the colour neutralisation of projectile remnants or a multi-parton interaction. The spectrum of underlying event particles is much softer and the soft part is considered to be a background from the jet's perspective. Various methods for correcting jet p_{T} spectra for soft background effects have been devised.

The correction to the p_{T} of the jets is done on an event-by-event basis where the corrected jet p_{T} is

$$p_{\mathrm{T}}^{\mathrm{jet}} = p_{\mathrm{T,rec}}^{\mathrm{jet}} - A^{\mathrm{jet}}\rho, \tag{1.23}$$

where $p_{\mathrm{T,rec}}^{\mathrm{jet}}$ is the uncorrected jet p_{T} , A^{jet} is the jet area and ρ is the medium background density per unit area. This method of background subtraction thus introduces two new parameters [27]. The first one represents the susceptibility of a jet to contamination by a soft background. This is embodied in the parameter called the *jet area* A^{jet}. Jets, as defined in the sections above, are composed of point-like objects and thus have no area. A jet area is therefore defined by introducing infinitely soft (negligible p_{T}) —*ghost particles.* Ghost particles have a definite area thus when they are clustered by the jet algorithm to a jet, they define its area. Note that IR safety is crucial in this procedure because the ghost particles must not change the composition of real jets. The jet area can vary significantly from the intuitive area of a cone jet equal to πR^2 [28]. It depends on the jet algorithm used as well as on the individual composition of each jet. The second parameter is the medium background p_{T} density per unit area ρ which can be estimated by various methods. The standard area based approach [28], its modification by the CMS [29] collaboration and a naive approach based on perpendicular cones are described further.

The background can only be removed on average. The jet $p_{\mathrm{T,rec}}^{\mathrm{jet}}$ is corrected, according to (1.23), only for mean background. This correction does not account for the local fluctuations in the background which further smear the jet p_{T}. These effects need to be corrected by unfolding.

As mentioned before, the preferred jet algorithm for the clusterisation of background jets is the k_{T} algorithm because it clusters soft particles first and is therefore more sensitive to the soft background. Thus the standard area based and CMS approaches to the ρ estimation operate on k_{T} jets.

1.8.1 Standard area based approach

In this method, the background density is estimated based on the observation that the ratio of the jet transverse momentum $p_{\mathrm{T,rec}}^{\mathrm{jet}}$ and the jet area A^{jet} behaves in two distinct ways for hard and soft jets. For hard jets, the ratio $\frac{p_{\mathrm{T,rec}}^{\mathrm{jet}}}{A^{\mathrm{jet}}}$ is large compared to soft jets where the ratio is close to ρ [28]. Therefore the medium background density is estimated as

$$\rho = \underset{i \in N}{\mathrm{median}} \left\{ \frac{p_{\mathrm{T,rec},i}^{\mathrm{jet}}}{A_i^{\mathrm{jet}}} \right\}, \tag{1.24}$$

where N is the set of all jets in an event.

This method underestimates the background in sparsely populated events such as a $\mathrm{p}+\mathrm{p}$ collision since the median can be dominated by contributions of ghost-particle jets for which $p_{\mathrm{T,rec}}^{\mathrm{jet}}$ is zero. It is therefore convenient to pick a large R parameter in order for the median to be non-zero.

1.8.2 CMS background

In light systems such as the $\mathrm{p}+\mathrm{p}$ collision with a low average charged-particle multiplicity, large parts of the detector do not contain physical jets and are covered only by ghost jets. In the standard area based method, ghost jets contribute to the background density as $\frac{p_{\mathrm{T,rec},i}^{\mathrm{jet}}}{A_i} = 0$ and events with a majority of ghost jets have zero ρ. This is corrected in [29] by modifying (1.24) to

$$\rho^{\mathrm{CMS}} = \underset{i \in M}{\mathrm{median}} \left\{ \frac{p_{\mathrm{T,rec},i}^{\mathrm{jet}}}{A_i} \right\} \cdot \frac{A^{\mathrm{phys}}}{A^{\mathrm{all}}}, \tag{1.25}$$

where A^{phys} is the area covered by physical jets only and A^{all} is the area covered by all jets. Physical jets are jets with at least one real particle. Furthermore, the median is constrained to physical jets M only.

1.8.3 Perpendicular cone background

Another method that can be used to estimate the local p_{T} background density is based on the p_{T} density in cones that are perpendicular to the leading jet in azimuth. First the leading jet (the jet with the highest p_{T}) in an event is found. Then, two cones perpendicular to the leading jet in azimuth and with the same pseudorapidity are constructed. This approach is based on the assumption that the region defined by the perpendicular cones is expected to be occupied by very few particles directly correlated with the leading jet. In a 2 → 2 process the resulting jets

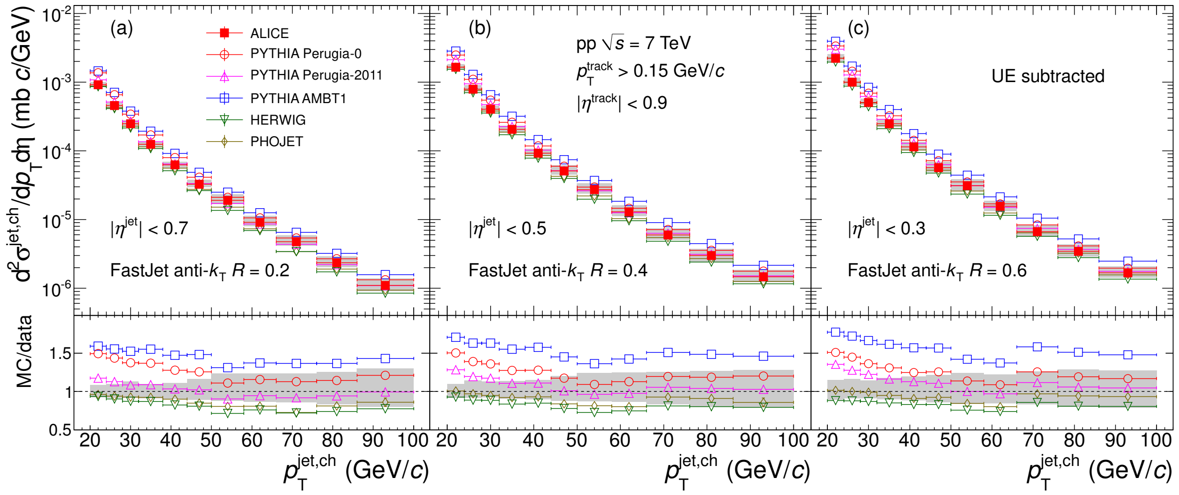

Figure 1.13: **Top panels:** Charged jet cross sections measured in the ALICE experiment in p+p collisions at $\sqrt{s} = 7$ TeV compared to several MC generators: PYTHIA AMBT1, PYTHIA Perugia-0 tune, PYTHIA Perugia-2011 tune, HERWIG, and PHOJET. **Bottom panels:** Ratios MC/Data. Shaded bands show quadratic sum of statistical and systematic uncertainties on the data drawn at unity [30].

are expected to be balanced in azimuth due to the conservation of momentum. The background is then given by

$$\rho^{\text{cone}} = \frac{p_{\text{T}}^{\text{sum}}}{2\pi R^2}, \tag{1.26}$$

where $p_{\text{T}}^{\text{sum}}$ is the summed p_{T} of all tracks that fall into the two cones and R is the radius of the cones. The area of the cones has to be chosen large enough, typically R can be set to 0.4. This method may overestimate the background in case of an event with more than two correlated jets, like a 2 → 3 process, and in the case that the jets are not precisely balanced in azimuth due to the intrinsic jet k_{T} [12]. This method is also more sensitive to the local fluctuations of the underlying event because it only studies a restricted part of the whole event.

The comparison of ρ of the three aforementioned approaches for p + p collisions at $\sqrt{s} =$ 13 TeV is shown in section 3.3.

1.9 p+p jet p_{T} spectra measurements in ALICE

Jet p_{T} spectra offer a unique tool for studying various aspects of QCD. At present, there are many different MC generators which allow to simulate particle production in p + p collisions. In the paper [30], the ALICE collaboration compared how these generators reproduce the measured inclusive spectra of charged jets measured in p + p collisions at $\sqrt{s} = 7$ TeV. Jets spectra were reconstructed for different jet resolution parameters. The models show large variations from the measured data. The comparison is shown in Figure 1.13.

In an other paper, ALICE compared 2.76 TeV spectra with NLO codes and has shown that in order to describe the data hadronization has to be considered [31]. The comparison is shown in Figure 1.14.

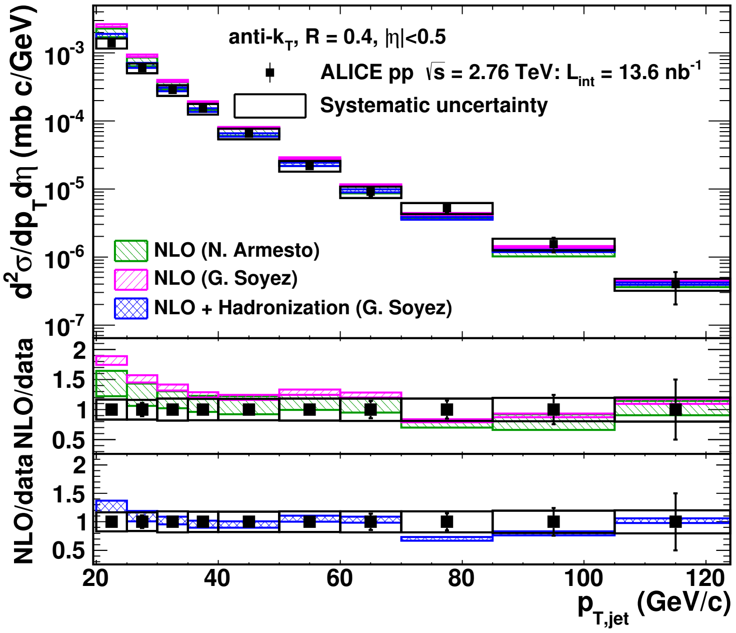

Figure 1.14: **Top panel:** Inclusive differential jet cross sections for jets with $R = 0.4$. Vertical bars show the statistical error, while boxes show the systematic uncertainty. The color bands show the NLO pQCD calculations discussed in [31].

Chapter 2

Experimental setup

2.1 The Large Hadron Collider

The **L**arge **H**adron **C**ollider [32] is a particle accelerator located at the European Organisation for Nuclear Research (CERN) in Geneva Switzerland. The LHC is the world's largest circular accelerator. It accelerates protons and lead nuclei in ultrahigh vacuum in two beams in opposite directions. These beams cross at four places with four large experiments (ATLAS, ALICE, CMS, LHCb) built around these interaction points. Particles are guided through the ring using superconducting electromagnets cooled by superfluid helium to 1.9 K. The beam pipes cross at four interaction points where large experiments have been built to observe the collisions. The LHC was built for better understanding unsolved questions in high energy physics by colliding particles at unprecedented energies and luminosities.

The acceleration of protons in the LHC is a multi-step process consisting of several stages [33]. First, an electric discharge removes the electron from hydrogen atoms leaving only hydrogen nuclei—protons. These are then accelerated in a linear accelerator *Linac 2* which accelerates them to 50 MeV. The protons are then injected into the *Proton Synchrotron Booster*— a circular accelerator that accelerates them to 1.4 GeV. The chain continues with the *Proton Synchrotron* and the *Super Proton Synchrotron* which accelerate the protons to 25 GeV and 450 GeV respectively. The Super Proton Synchrotron then injects the particles into the LHC which as of 2017 accelerates protons to a maximum energy of 6.5 TeV. The accelerator chain is depicted in Figure 2.1.

2.2 A Large Ion Colliding Experiment

A **L**arge **I**on **C**olliding **E**xperiment is an experiment located at the 2nd interaction point of the LHC. Its main purpose is the study of Quark Gluon Plasma— a state of matter created in high energy heavy physics ion collisions. Besides the heavy-ion program, ALICE has a rich $\mathrm{p}+\mathrm{p}$ program.

The ALICE detector [35] consists of a central barrel and a forward muon arm. The central barrel is placed in the $L3$ magnet which supplies a 0.5 T magnetic field. The interaction point is situated in the centre of the central barrel. The detectors surrounding the interaction point are dedicated to track reconstruction and identify the outgoing particles. The three detectors that are of importance to this analysis shall be discussed further. The schematic depiction of ALICE is in Figure 2.2.

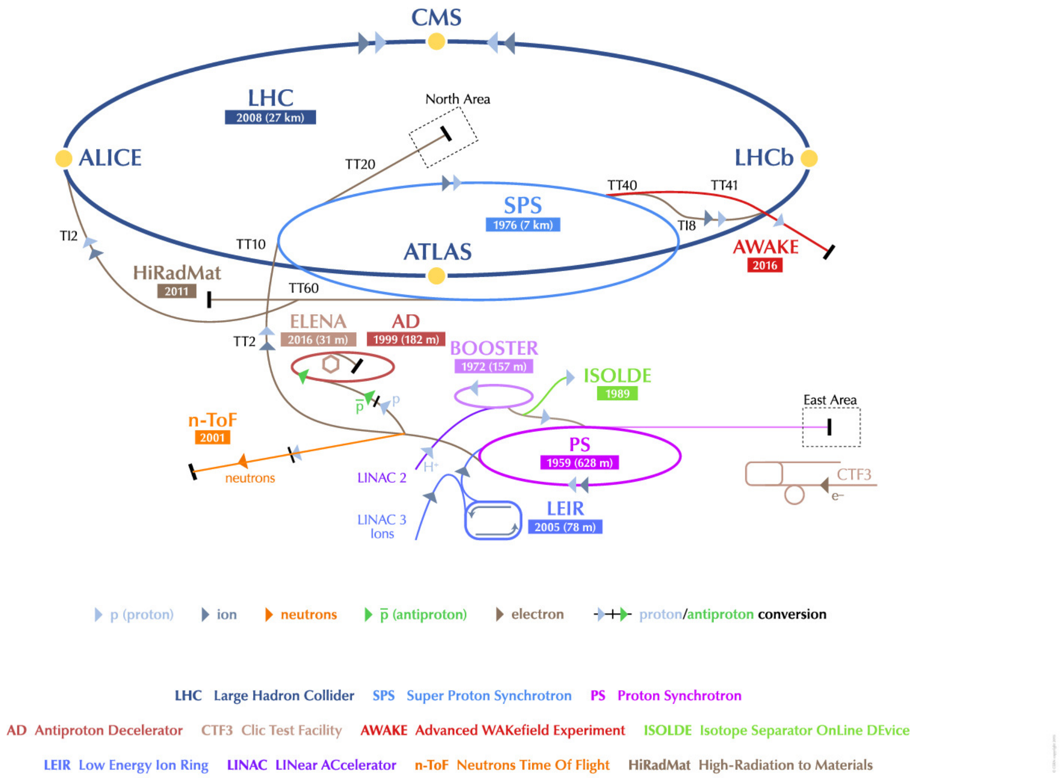
CMS
LHC
2008 (27 km)
North Area
ALICE
TT20
LHCb
TT40
TT41
SPS
1976 (7 km)
TI8
TI2
TT10
ATLAS
AWAKE
2016
HiRadMat
2011
TT60
ELENA
2016 (31 m)
AD
1999 (182 m)
TT2
BOOSTER
1972 (157 m)
ISOLDE
1989
p̄
p
East Area
n-ToF
2001
PS
1959 (628 m)
H⁺
CTF3
e⁻
neutrons
LINAC 2
LINAC 3
Ions
LEIR
2005 (78 m)
p (proton)
ion
neutrons
p̄ (antiproton)
electron
proton/antiproton conversion
LHC Large Hadron Collider
SPS Super Proton Synchrotron
PS Proton Synchrotron
AD Antiproton Decelerator
CTF3 Clic Test Facility
AWAKE Advanced WAKefield Experiment
ISOLDE Isotope Separator OnLine DEvice
LEIR Low Energy Ion Ring
LINAC LINear ACcelerator
n-ToF Neutrons Time Of Flight
HiRadMat High-Radiation to Materials

Figure 2.1: The schematics of the accelerators and beamlines in CERN [34].

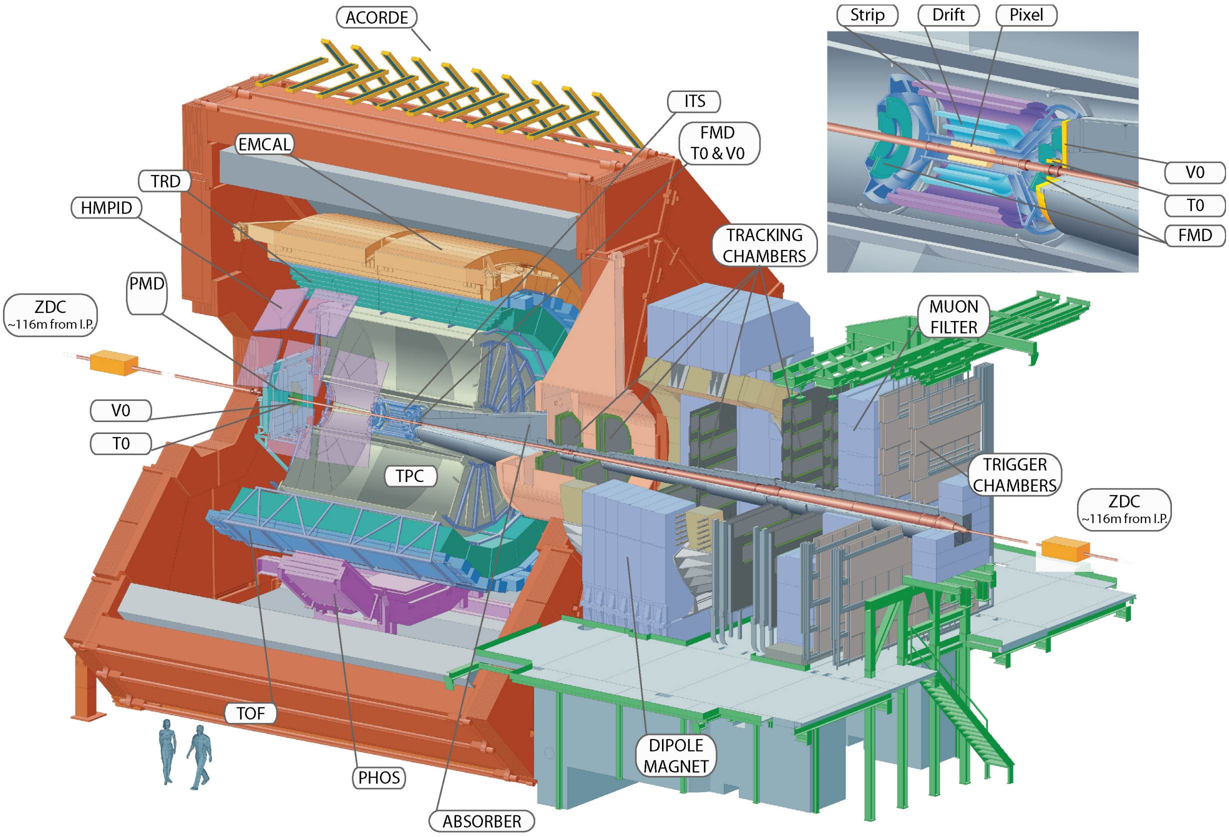
ACORDE
Strip
Drift
Pixel
ITS
FMD
T0 & V0
EMCAL
TRD
HMPID
V0
T0
FMD
TRACKING CHAMBERS
PMD
ZDC
~116m from I.P.
MUON FILTER
V0
T0
TPC
TRIGGER CHAMBERS
ZDC
~116m from I.P.
TOF
DIPOLE MAGNET
PHOS
ABSORBER

Figure 2.2: The schematic depiction of the ALICE experiment at the LHC. The detail of the ITS and the forward detectors is seen in the upper right corner. The L3 magnet is coloured red.

2.2.1 Inner Tracking System (ITS)

The ITS [36] is the closest detector to the interaction point and consists of six cylindric layers of silicon detectors. Silicon Pixel Detectors (SPD) are the two innermost layers. The middle two layers consist of Silicon Drift Detectors (SDD). The two outermost layers are Silicon Strip Detectors (SSD). Each of the six layers is centred around the vertex diamond and the beam goes through the axis. The radii of the layers are 3.9, 7.6, 15.0, 23.9, 38.0, 43.0 cm. The material budget of the ITS is about 8 % of the radiation length. The ITS covers the pseudorapidity range of $\eta \in (-0.9, 0.9)$. The first layer has a more extended pseudorapidity coverage $|\eta| < 1.98$ to provide, together with the Forward Multiplicity Detectors (FMD), continuous coverage for the measurement of charged particles multiplicity. The ITS is illustrated at the top right corner of Figure 2.2. Its purpose is to determine the position of the primary and secondary vertices in a collision and to aid tracking and particle identification.

2.2.2 Time Projection Chamber (TPC)

The TPC [37], seen in Figure 2.2 in grey around the ITS, is the main detector in ALICE that provides tracking and PID (particle identification based on $\mathrm{d}E/\mathrm{d}x$). It is a cylinder with an inner radius of 85 cm, an outer radius of 250 cm and a length of 500 cm. It is filled with the mixture of $\mathrm{He/CO_2}$ which has to be kept at a constant temperature with fluctuations smaller than 0.1 K in order to minimise the dependence of multiple scattering in the gas on temperature. The electrostatic field in the TPC is generated by a central cathode and end plate cap anodes with the potential gradient 400 V/cm. This electric field is collinear with the magnetic field of the $L3$ solenoid. A particle propagating through the chamber ionises the gas which produces electron-ion pairs. Ions drift to the central electrode and electrons drift in the electromagnetic field to the multi-wire proportional chambers at the end caps of the TPC. These electrons provide the x and y coordinates in the transverse plane to the beam axis of the vertex point where the ionisation occurred. The z coordinate is obtained from the drift time.

2.2.3 V0

The V0 [38] detector consists of two rings of plastic scintillators V0A at forward, $2.8 < \eta < 5.1$, and V0C at backward, $-3.7 < \eta < -1.7$ pseudorapidities. V0A is 340 cm from the centre of the detector and V0C 90 cm. This asymmetry is caused by an absorber in the muon arm. Both disks are segmented into 32 individual scintillators placed in 4 concentric rings. The V0 detector is used for triggering and measurement of centrality and reaction plane angle. Its location can be seen in Figure 2.3.

2.2.4 Computational infrastructure

The analysis has been carried out in the *AliRoot* software [39]. It is built on the *C++* framework called ROOT [40]. The computation has been carried out on the CERN grid [41].

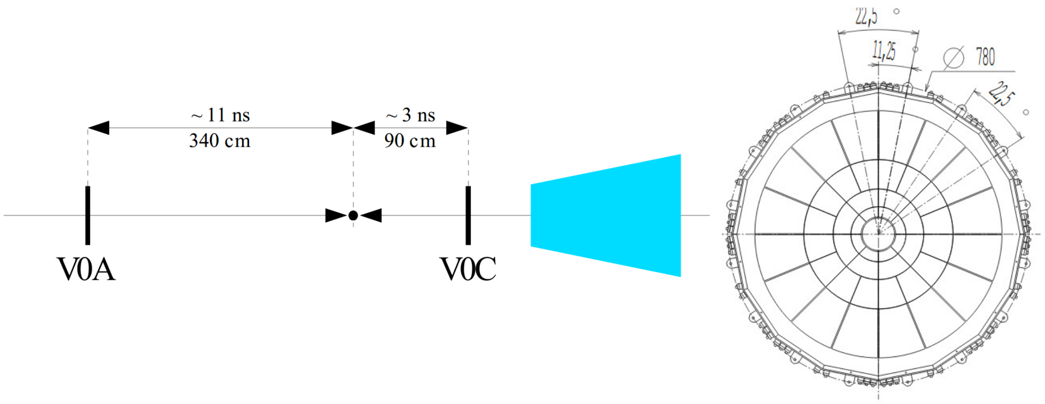
~ 11 ns
340 cm
~ 3 ns
90 cm
V0A
V0C
22,5 °
11,25
∅ 780
22,5 °

Figure 2.3: **Left:** The location of the V0A and V0C detector with respect to the interaction point marked by a dot. The blue trapezoid represents the absorber in front of the muon arm. **Right:** The shape of the V0 detectors. Taken from [38].

Chapter 3

Analysis of p_{T} spectra of inclusive charged jets in $\mathrm{p}+\mathrm{p}$ collisions at $\sqrt{s} = 13$ TeV

The goal of this thesis is to analyse inclusive p_{T} spectra of charged anti-k_T jets produced in $\mathrm{p}+\mathrm{p}$ collisions at $\sqrt{s} = 13$ TeV in ALICE. This chapter specifies event selection, track selection criteria and jet reconstruction.

The analysis is based on data from 2016 (period *2016l*). The $\mathrm{p}+\mathrm{p}$ data from 2015 (period *2015f*) has initially been considered however it did not pass the criteria for uniformity in detector efficiency as shown later. The analysed run numbers from *2015f* and *2016l* are quoted in Table 3.1.

2015f:	226085, 226170, 226175, 226176, 226177, 226183, 226208, 226210, 226212, 226217, 226220, 226225, 226444, 226445, 226452, 226466, 226468, 226472, 226476, 226483, 226495, 226500, 226532, 226543, 226551, 226554, 226569, 226573, 226591, 226593, 226596, 226600, 226602, 226603, 226605, 226606
2016l:	259389, 259394, 259395, 259396, 259473, 259477, 259649, 259650, 259668, 259697, 259700, 259703, 259704, 259705, 259711, 259713, 259747, 259748, 259750, 259751, 259752, 259756, 259781, 259788, 259789, 259822, 259841, 259842, 259860, 259866, 259867, 259868, 259888, 260010, 260011, 260014

Table 3.1: Analysed run numbers.

3.1 Event selection

The *V0AND* trigger has been used to trigger events. This trigger requires a time coincidence in the opposite *V0A* and *V0C* scintillation detectors to trigger an event.

The quality of the selected primary interaction vertex and its position is constrained by means of several criteria listed in the *AliRoot* function *AliAnalysisUtils::IsVertexSelected2013pA()*. Events that pass the vertex cut must satisfy these conditions

1. The primary vertex must be reconstructed with at least one contributor

	Before cuts	After cuts
2015f	7.96×10^7	6.66×10^7
2016l	4.43×10^7	4.02×10^7

Table 3.2: The number of events that survived the different cut stages.

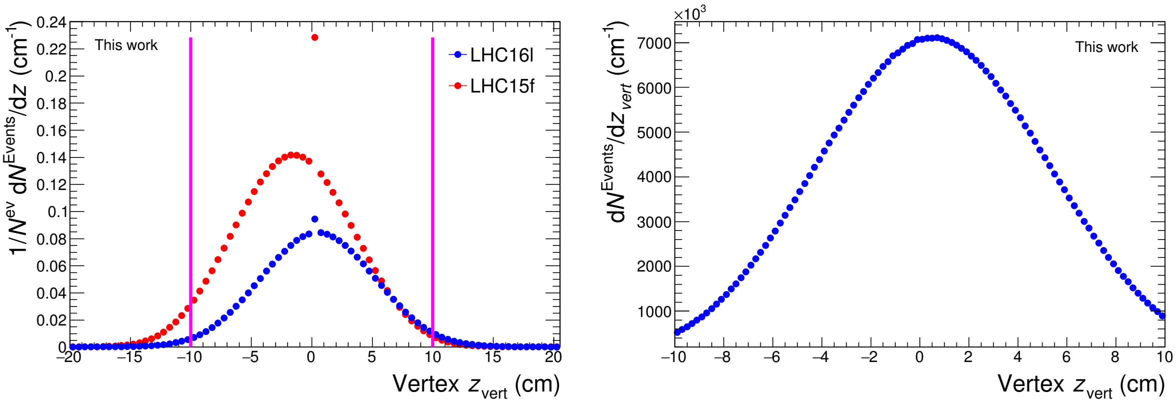

Figure 3.1: **Left:** The z-distribution of the primary vertex before event selection cuts. Magenta lines indicate the position of the vertex cut. The spike at $z_{\text{vert}} = 0$ comes from events with no reconstructed vertices. Events from *2016l* are marked by blue circles and events from *2015f* by red circles. **Right:** The z-distribution of the primary vertex after event selection cuts for the *2016l* period.

2. The primary vertex must be reconstructed using data from the SPD
3. The deviation of the z coordinate of the vertex z_{vert} must be within 10 cm from the centre of the detector
4. If the vertex was reconstructed with a fallback vertex finder the errors have to be small

At high collision rates it is possible that several collisions occur in the same bunch crossing and overlap in the detector. This is known as *pile up* and needs to be corrected in the analysis. The pile up cut is carried out by the *AliRoot* function *AliAnalysisUtils::IsPileUpEventFromSPD()*. The numbers of events that survived the pileup and vertex cuts are shown in Table 3.2. Figure 3.1 shows the distribution of the z-vertex for events before the vertex cut is applied.

3.2 Track selection

In order to ensure uniform azimuthal track distribution, which is essential for the analysis of jets, so-called *hybrid tracks* are used [42]. Hybrid tracks consist of higher quality *global tracks* and lower quality *complementary tracks*. The conditions that global and complementary tracks have to satisfy are

- Require TPC refit. The ALICE track reconstruction can be described as follows. Tracks are first reconstructed using TPC points extrapolated inwards to the SPD. Then an outward track reconstruction is done starting from SPD. The third step is the TPC refit which refits the tracks in the TPC [39].

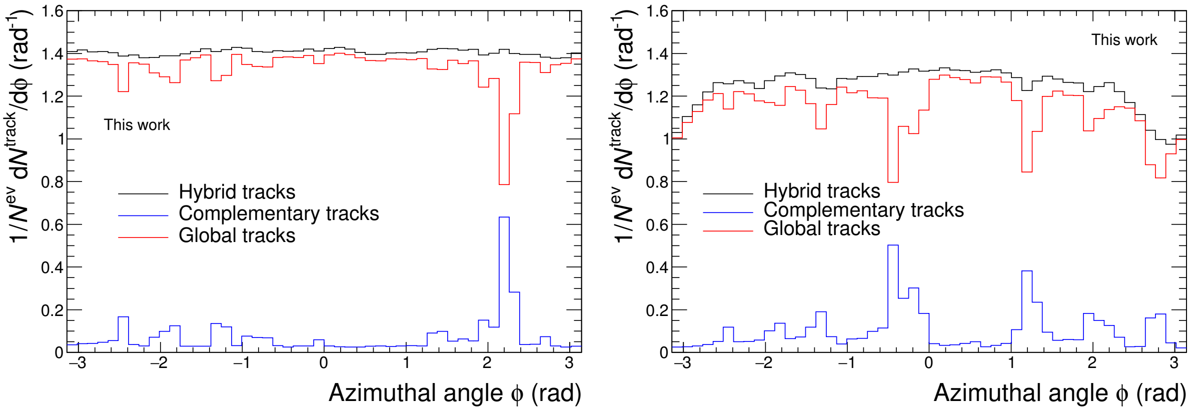

Figure 3.2: Hybrid track composition normalised per the number of events and bin width. **Left**: *2016l*. **Right**: *2015f*

- Crossed row cuts in the TPC. The end caps of the TPC consist of 159 pad rows. Only tracks which have at least 70 rows crossed are accepted.
- The maximum fraction of shared TPC clusters should be 40%.
- χ^2 on each of reconstructed TPC and ITS clusters should be at most 4.
- $\chi^2 < 36$ for global constrained tracks.
- Tracks that have a kink in the TPC are rejected.
- Transverse momentum cut: $p_{\mathrm{T}}^{\mathrm{track}} > 150$ MeV$/c$. This is to ensure sufficient reconstruction efficiency.
- Pseudorapidity cut: $|\eta^{\mathrm{track}}| < 0.9$. This is to ensure a uniform acceptance and efficiency of reconstruction.
- For global tracks: Demand ITS refit and at least one hit in SPD.
- For the complementary tracks: No ITS refit or SPD hits are required.

The composition of tracks can be seen in Figure 3.2. The tracks in the period *2015f* are composed of 91.75 % global tracks and in the period *2016l* global tracks constitute 94.89 % of the total.

The efficiency $\mathcal{E}$ of the reconstruction of tracks can be estimated using Monte Carlo simulations. This is done by introducing the notion of *primary* and *fake* tracks. Physical primary tracks correspond to particles from electromagnetic or strong decays [43]. This is due to the fact that these particles have very short lifetimes and therefore do not propagate far from the primary vertex before decaying. Fake primary tracks are tracks that originated in a weak decay or are reconstructed from segments of different particles.

The cuts in the analysis are tuned to preferentially suppress the number of fake tracks and keep primary tracks. The probability that a primary track will pass the cuts is determined by the reconstruction efficiency which is estimated as

$$\mathcal{E} = \frac{N_{\mathrm{rec}}\left(p_{\mathrm{T}}^{\mathrm{part}}\right)}{N_{\mathrm{prim}}\left(p_{\mathrm{T}}^{\mathrm{part}}\right)}, \tag{3.1}$$

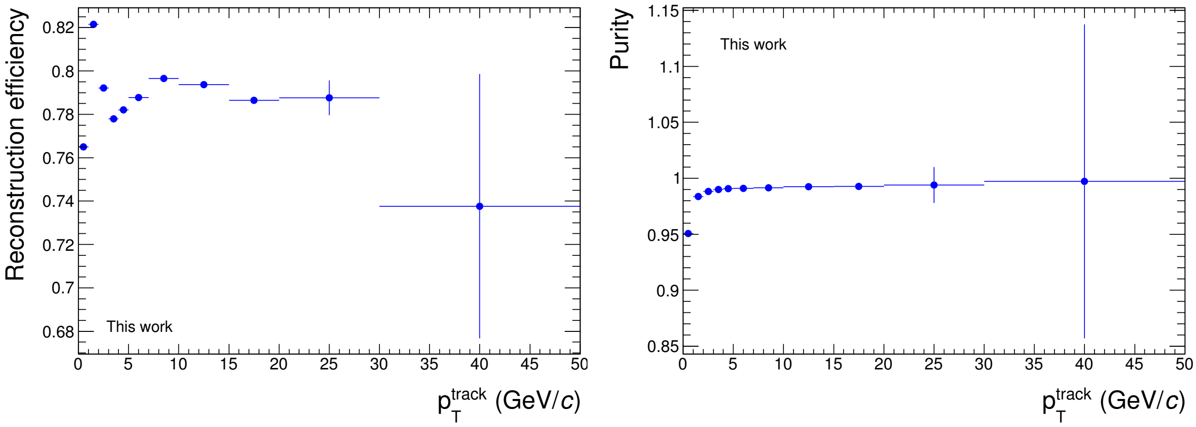

Figure 3.3: **Left**: The efficiency of track reconstruction for the period *2016l* based on the Monte Carlo simulation *2016j2a2*. **Right**: The purity of reconstructed tracks in *2016l* based on the Monte Carlo simulation *2016j2a2*.

where N_{rec} is the number of true primary particles reconstructed by the detector and N_{prim} is the number of generated tracks and $p_{\mathrm{T}}^{\mathrm{part}}$ is the transverse momentum of particles from the event generator i.e. the p_{T} not affected by the detector. The purity $\mathcal{P}$ of the reconstructed tracks is obtained as

$$\mathcal{P} = \frac{N_{\mathrm{rec}}\left(p_{\mathrm{T}}^{\mathrm{part}}\right)}{N_{\mathrm{rec}}\left(p_{\mathrm{T}}^{\mathrm{part}}\right) + N_{\mathrm{fake}}\left(p_{\mathrm{T}}^{\mathrm{det}}\right)}, \tag{3.2}$$

where N_{fake} is the number of fake tracks reconstructed by the detector and $p_{\mathrm{T}}^{\mathrm{det}}$ is the p_{T} assigned to the particle by the reconstruction. The reconstruction efficiency and purity of tracks estimated from PYTHIA 6 Perugia 11 Monte Carlo simulation (MC dataset*2016j2a2*) for the period *2016l* is seen in Figure 3.3. The efficiency of track reconstruction is approximately 80 % for particles with $p_{\mathrm{T}} > 5$ GeV/c. The reconstruction efficiency for particles below 5 GeV/c is affected by the bending of tracks in the magnetic field which can then pass through inefficient regions in ALICE (e.g. sector borders in TPC). The purity of tracks with $p_{\mathrm{T}} > 1$ GeV/c is better than 98 %.

3.3 Jet selection

Jets are reconstructed from charged tracks using the k_{T} and anti-k_{T} algorithms with $R = 0.4$. *FastJet-v3.1.3* [24] has been used for the clusterisation of jets. In order to eliminate jets that have been effected by the loss of particles that fall outside the detector acceptance further cut on the jet pseudorapidity is applied. Such jets would have a naturally reduced p_{T}. The pseudorapidity of jets has to satisfy $|\eta^{\mathrm{jet}}| < 0.9 - R$ where R is the jet resolution parameter roughly measuring the radius of the jet cone. Tracks are assumed to correspond to massless particles. Their 4-momenta were added using the recombination $E-$scheme [24]. The used ghost area is 0.01.

3.4 Data quality assurance

Before the analysis of p_{T} spectra can be carried out it is necessary to check that the conditions for data taking in each run were similar. The stability of tracking can be conveniently checked by inspecting the mean track multiplicity on a run-by-run basis together with the corresponding pseudorapidity and azimuthal angle distributions of reconstructed tracks.

3.4.1 Period *2015f*

The mean run-by-run track multiplicity of the *2015f* dataset is seen in Figure 3.4. Runs with zero mean track multiplicity have to be excluded from further analysis. Further abnormalities are marked by red arrows and an ellipse in Figure 3.4. A closer examination of these runs reveals problems with the detectors.

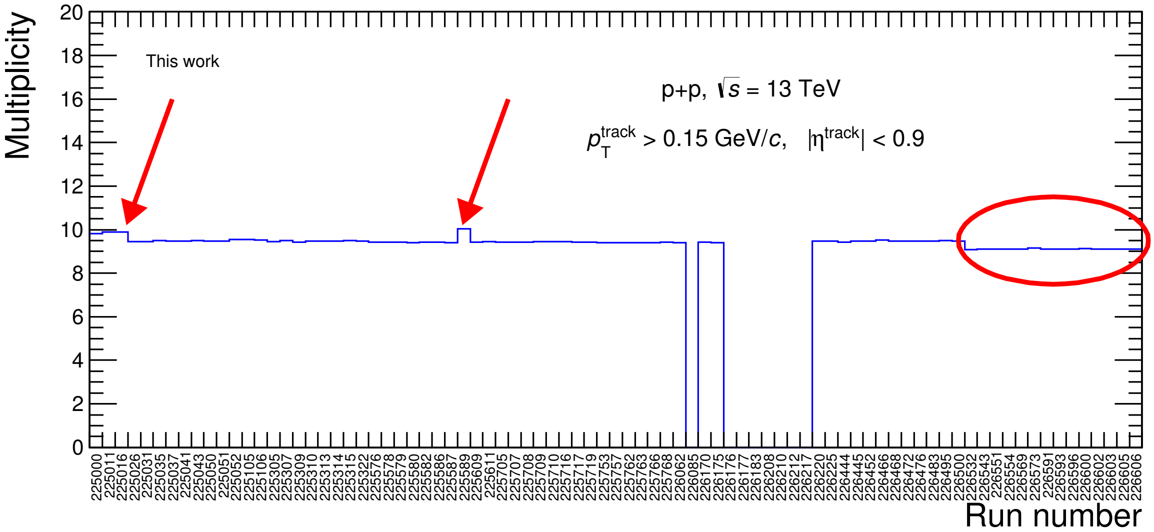

Figure 3.4: Average track multiplicity versus the run number in the whole *2015f* period.

Figure 3.5 shows a comparison of per event normalised pseudorapidity distributions of charged tracks with $p_T > 150$ MeV$/c$ of produced tracks in three runs that are representatives of each of the three regions. The set *225011* is a sample from the higher multiplicity region, the set *225709* is a sample set from the average multiplicity region and *226593* is a sample from the lower multiplicity region. Figure 3.5 exhibits an asymmetry in η. This asymmetry is not expected from physics since the collision system is symmetric. The azimuthal distribution, seen in Figure 3.6, further confirms strong irregularities in the detector efficiency, namely a large inefficiency region at $\phi = \pi$. In an ideal case, this distribution is supposed to be uniform because the ALICE detector is azimuthally symmetric. A jet analysis requires a uniform detector efficiency across the acceptance. If this condition had not been met the jet algorithm would preferentially create jets in the regions with higher reconstruction efficiency. The whole *2015f* dataset has therefore been excluded from all further analysis.

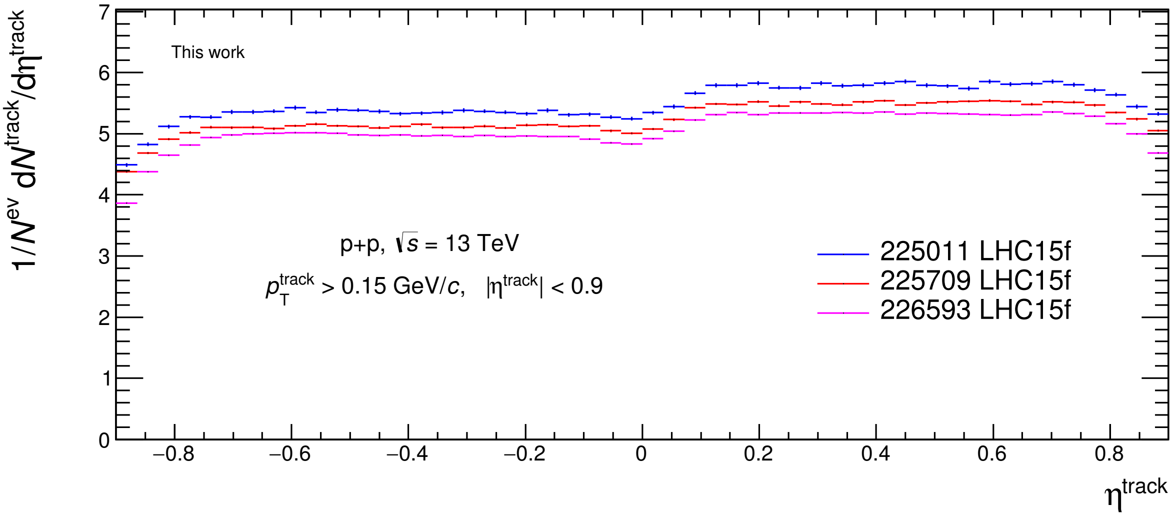

Figure 3.5: Comparison of the pseudorapidity distributions of tracks in runs representing three different regions from the *2015f* period. Distributions are normalised per event and bin width.

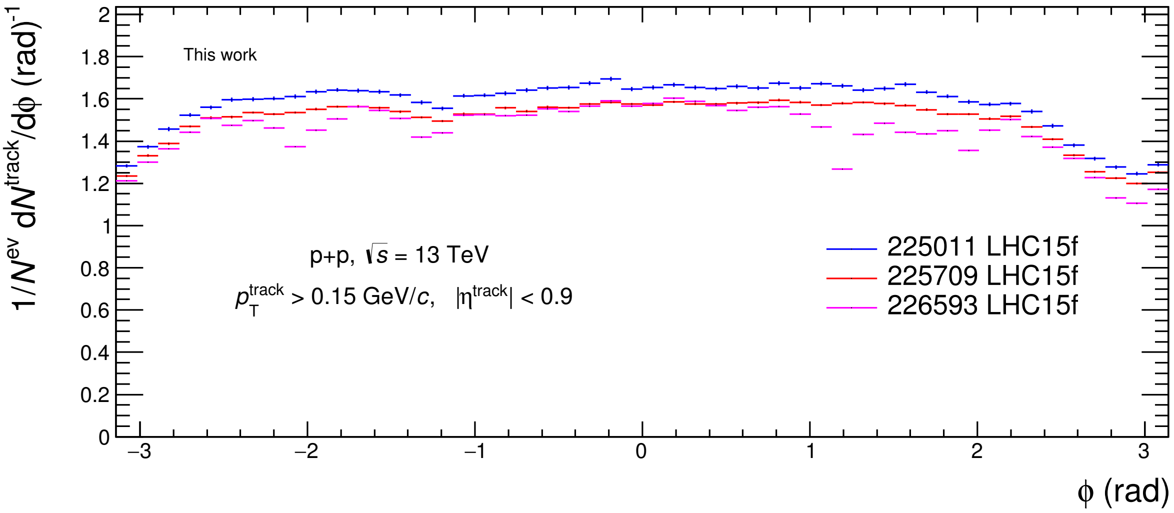

Figure 3.6: Comparison of the azimuthal distributions of tracks in runs representing three different regions from the *2015f* period. Distributions are normalised per event and bin width.

3.4.2 Period ***2016l***

The average charged track multiplicity is plotted in Figure 3.7.

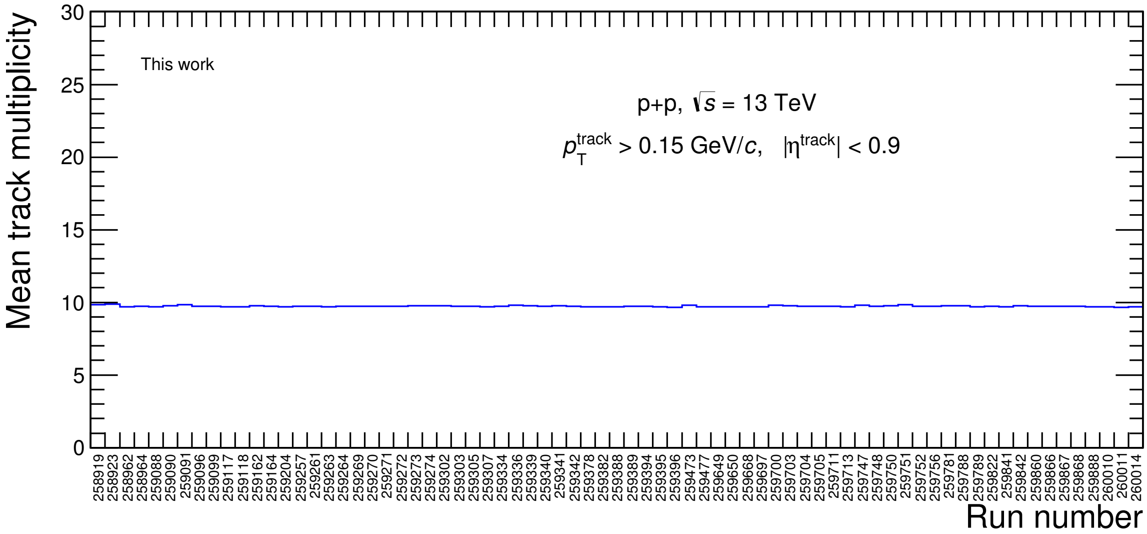

Figure 3.7: Average track multiplicity versus the run number in the whole *2016l* period.

Pseudorapidity and azimuthal distributions show no significant problems. An example comparison of two runs from *2016l* period is shown in Figures 3.8 and 3.9. The distributions are symmetric as expected. The dip in the pseudorapidity distribution at $\eta = 0$ is caused by the central electrode of the TPC.

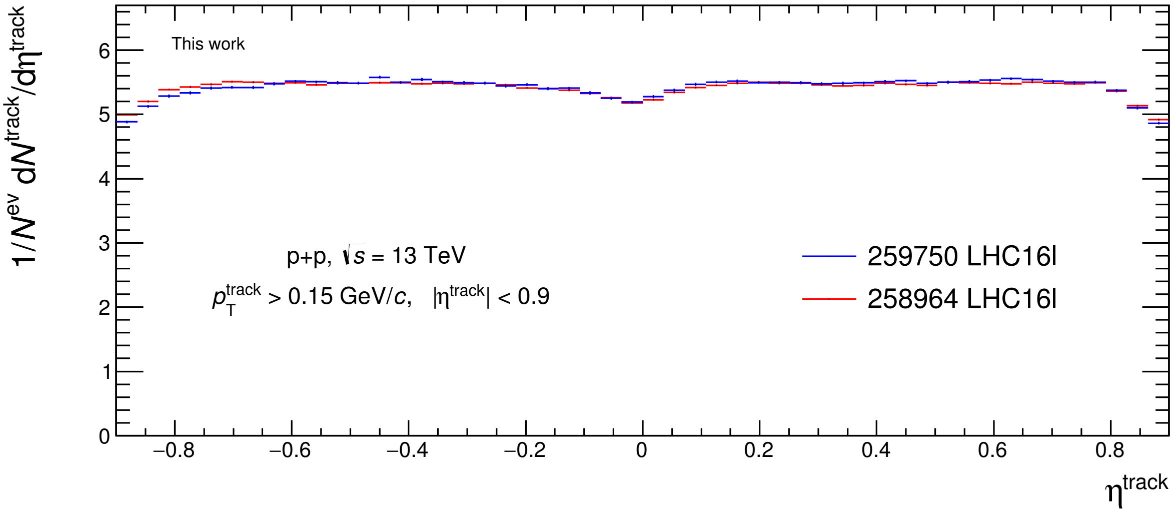

Figure 3.8: An example of the comparison of charged track pseudorapidity distributions of two datasets from the *2016l* period. Distributions are normalised per event and bin width.

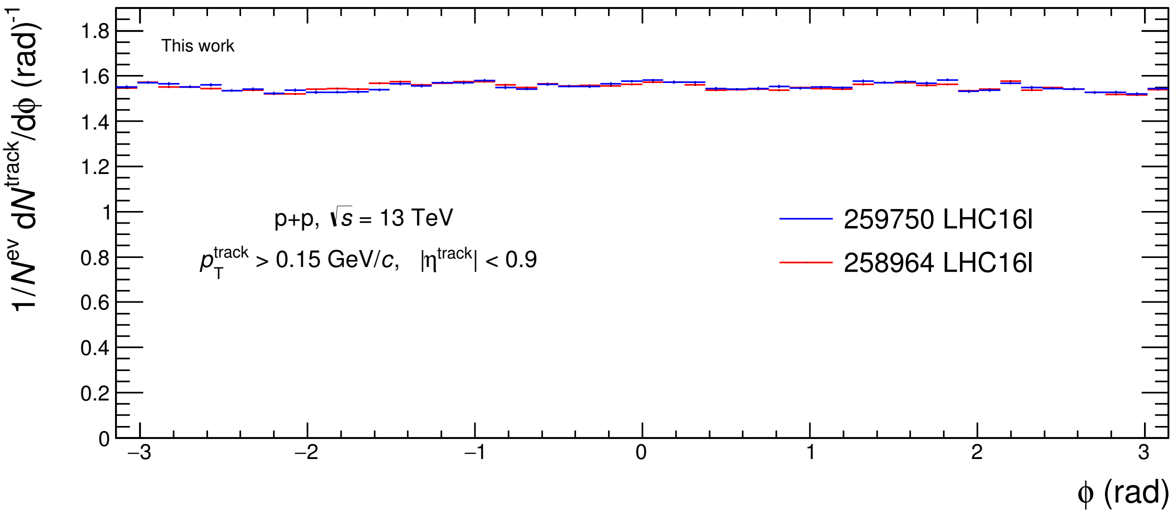

Figure 3.9: An example of the comparison of charged track azimuthal distributions of two datasets from the *2016l* period. Distributions are normalised per event and bin width.

The η distributions are falling at high pseudorapidities due to fewer cross rows of the TPC being crossed. None of the analysed runs exhibits a significant deviation from the average and all of them will be used to analyse p_{T} spectra of jets.

Chapter 4

Analysis of simulations

Simulations are used to correct the raw data for instrumental effects and to compare the corrected measurements to expectations from an event generator. Simulated p + p collisions at $\sqrt{s} = 13$ TeV events were generated using PYTHIA 6 [20] with the Perugia 11 tune. The generated PYTHIA events were processed with a detailed GEANT3 model of the ALICE detector and a model of the detector response which reflected the experimental situation for the *2016l* period. Subsequently these data were analysed as real data.

Simulated events, which include primary particles and the daughters of strong and electromagnetic decays but not secondaries from interactions in the detector material or the daughters of weak decays, are denoted as "particle level". Simulated events which also include instrumental effects and weak decay daughters, where reconstructed tracks are selected using the experimental cuts, are denoted as "detector level".

4.1 Simulated events anchored to runs from *2016l*

The simulated Perugia 11 events anchored to runs from *2016l* in the Monte Carlo data set *2016j2a2* were used. The *2016j2a2* simulation contains 4.08×10^7 simulated events of which 3.80×10^7 have passed the event selection. The average track multiplicity is shown in Figure 4.1.

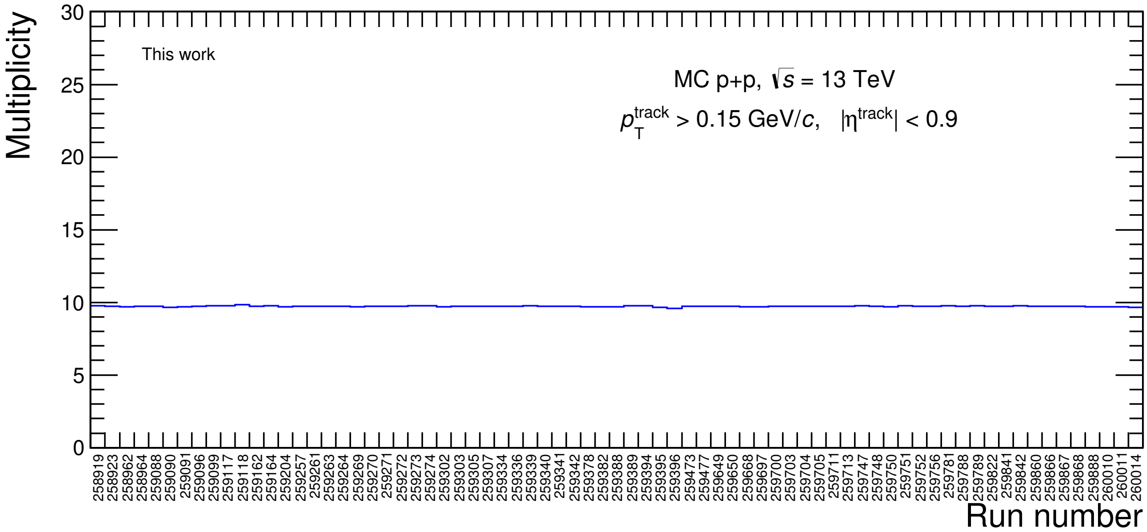

Figure 4.1: Average track multiplicity in the PYTHIA detector level simulation corresponding to the period *2016l* (MC data set *2016j2a2*).

The comparison of pseudorapidity and azimuthal angle distributions of the measured data and the corresponding Monte Carlo PYTHIA 6 Perugia 11 simulation *2016j2a2* anchored to *2016l* is shown in Figures 4.2 and 4.4 for $p_{\mathrm{T}} > 150$ MeV/c and for tracks with $p_{\mathrm{T}} > 3$ GeV/c in Figures 4.3 and 4.5.

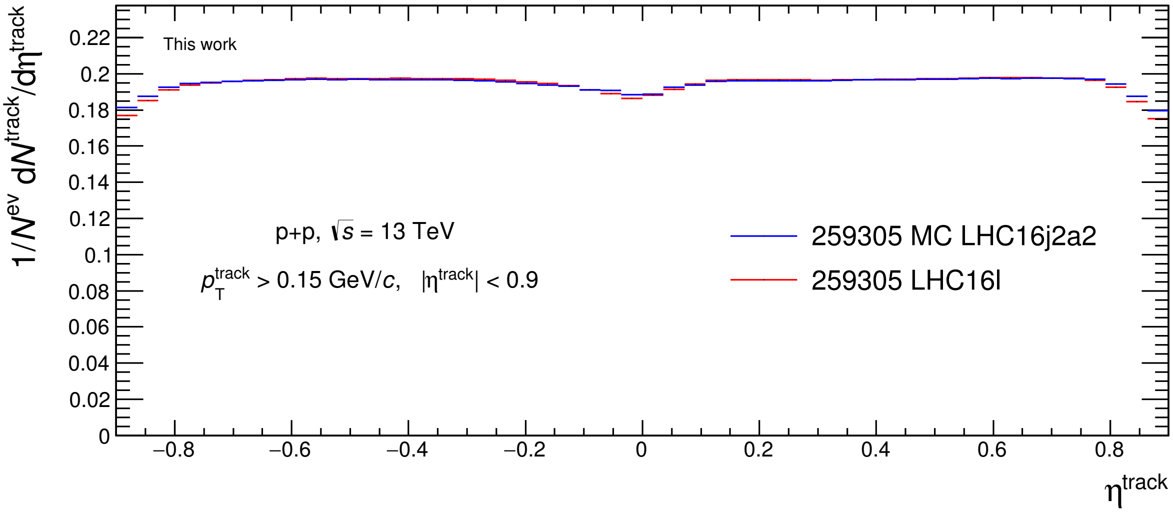

Figure 4.2: Pseudorapidity distributions of tracks with $p_{\mathrm{T}} > 150$ MeV/c from the Monte Carlo PYTHIA 6 Perugia 11 simulation *2016j2a2* anchored to *2016l*. Distributions are normalised per event and bin width. The corresponding run numbers are quoted in the legend.

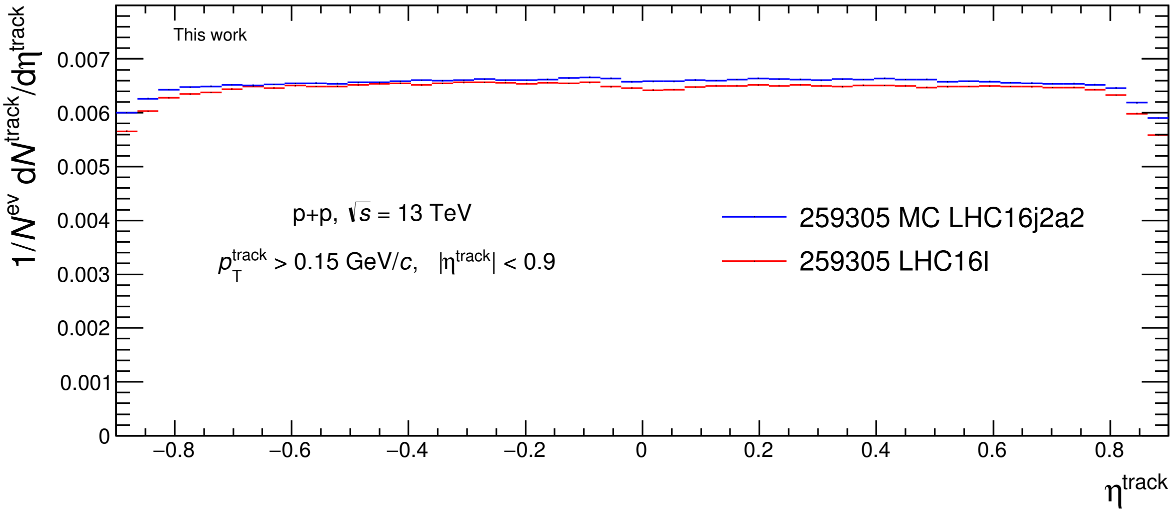

Figure 4.3: Pseudorapidity distributions of tracks with $p_{\mathrm{T}} > 3$ GeV/c from the Monte Carlo PYTHIA 6 Perugia 11 simulation *2016j2a2* anchored to *2016l*. Distributions are normalised per event and bin width. The corresponding run numbers are quoted in the legend.

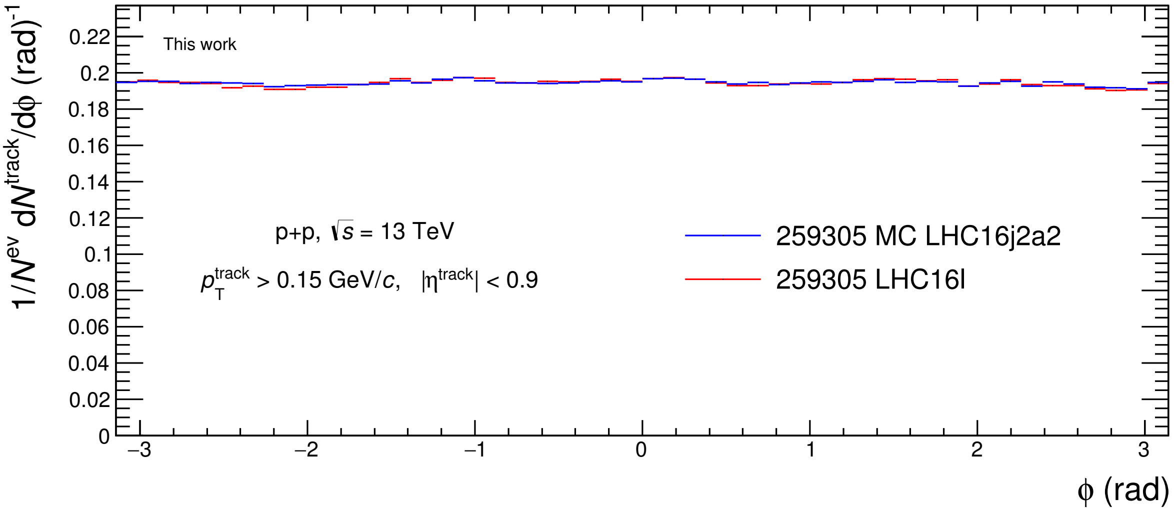

Figure 4.4: A comparison of azimuthal angle distributions of tracks with $p_{\mathrm{T}} > 150$ MeV/c of corresponding runs from *2016l* and *2016j2a2*. Distributions are normalised per event and bin width.

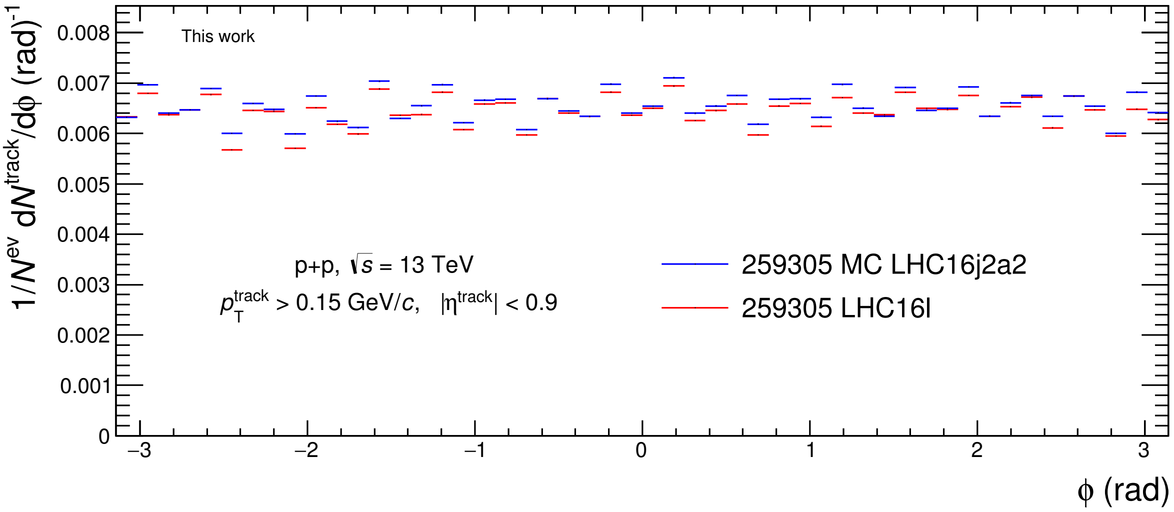

Figure 4.5: A comparison of azimuthal angle distributions of tracks with $p_{\mathrm{T}} > 3$ GeV/c of corresponding runs from *2016l* and *2016j2a2*. Distributions are normalised per event and bin width.

The MC simulations reproduce the measured spectra very well and are therefore going to be used in the subsequent analysis to estimate detector effects on the measured spectra of jets.

Chapter 5

Raw jet p_T spectra

In this chapter, inclusive, charged, anti-k_T, $R = 0.4$ jet p_T spectra from p + p collisions at $\sqrt{s} = 13$ TeV obtained form the period *2016l* are shown. The raw, unnormalised jet p_T spectrum is presented in Figure 5.1. This spectrum needs to be corrected for detector effects.

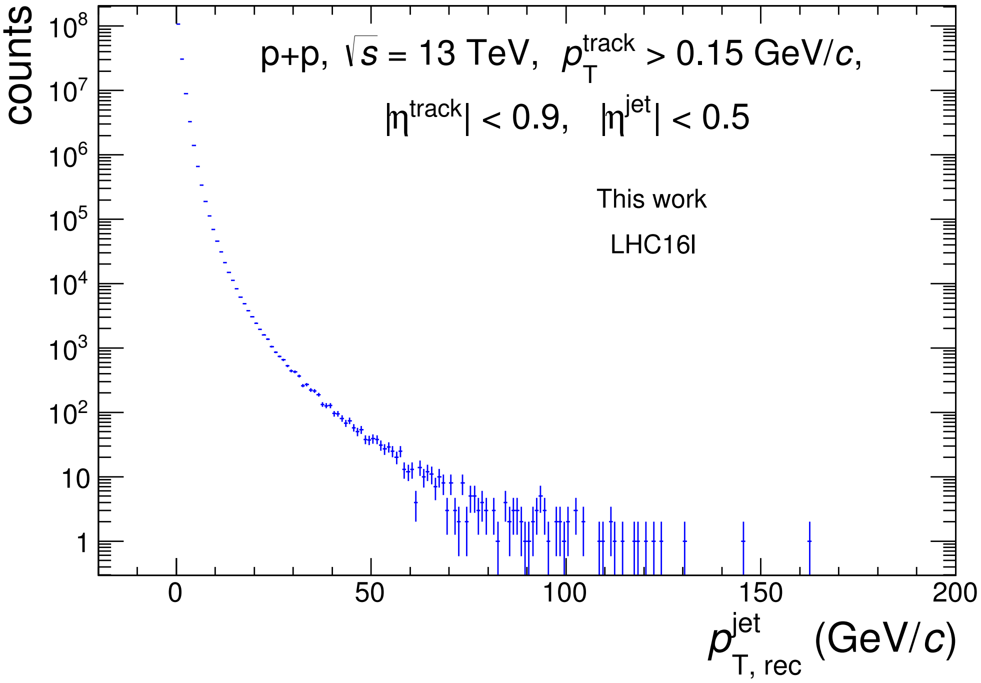

Figure 5.1: The unnormalised, raw, charged anti-k_T , $R = 0.4$ jet p_T spectrum from the period *2016l* with the bin width of 1 GeV/c. Measured in p+p collisions at $\sqrt{s} = 13$ TeV. Uncorrected for background

The corresponding unfolding procedure that corrects the spectrum for detector effects is more stable when the statistics in bins is large enough (ALICE analyses use at least 10 counts per bin). Therefore the spectrum is rebinned and a larger bin width in sparsely populated regions is used. The chosen binning for the raw spectrum is

$$p_\mathrm{T,\,rec}^\mathrm{jet} = \{5, 9, 13, 17, 21, 26, 32, 38, 50, 90\}\ (\mathrm{GeV}/c). \tag{5.1}$$

The spectrum after rebinning is shown in Figure 5.2.

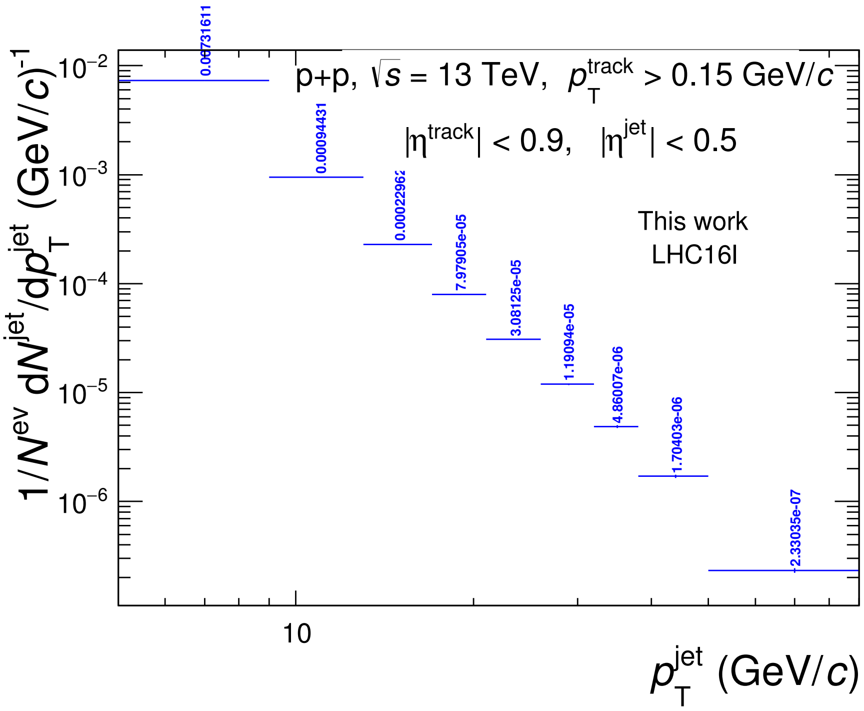

Figure 5.2: The unnormalised, raw, charged anti-k_{T} , $R = 0.4$ jet p_{T} spectrum from the period *2016l*. Measured in p+p collisions at $\sqrt{s} = 13$ TeV. The spectrum has been rebinned according to (5.1). The numbers above each bin give the number of counts.

In order to compare the measured raw spectrum to the particle level Monte Carlo spectrum, both spectra are normalised per the number of events and the bin width. The comparison is depicted in Figure 5.3.

The influence of the underlying event (UE) on the reconstructed jet p_{T} spectrum is shown in Figure 5.4 where the UE uncorrected and corrected spectra are compared. The background density ρ as well as the p_{T} correction $A^{\mathrm{jet}} \times \rho$ from the two methods is shown in Figure 5.5. The standard area-based approach subtracts on average a p_{T} value of 0.10 GeV/c, the CMS-improved method 0.39 GeV/c and the perpendicular cone method 0.31 GeV/c. This correction is negligible for jets in the considered p_{T} range and is thus not considered henceforth. Note that the naive cone method (shown in Figure 5.5) grossly overestimates the background since in an event with more than two jets, particles from a jet might intersect the fixed cones.

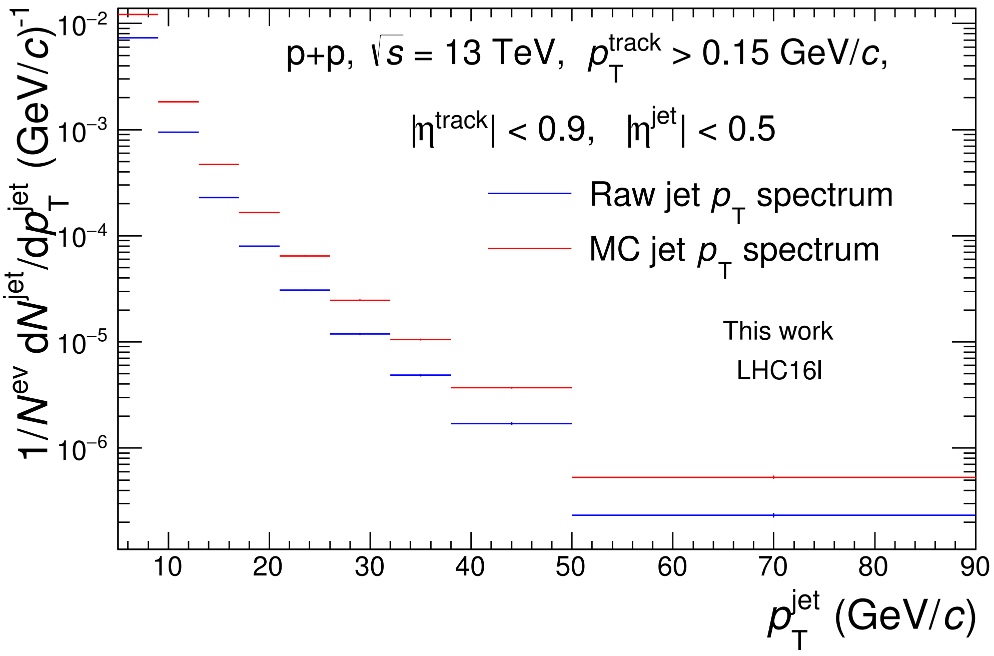

Figure 5.3: The per-event and per-bin-width normalised charged anti-k_T , $R = 0.4$ jet p_T spectra from the period *2016l* measured in p+p collisions at $\sqrt{s} = 13$ TeV and the corresponding particle level PYTHIA 6, Perugia 11. Monte Carlo simulation *2016j2a2*. The spectrum has been rebinned according to (5.1) and is not corrected for the UE.

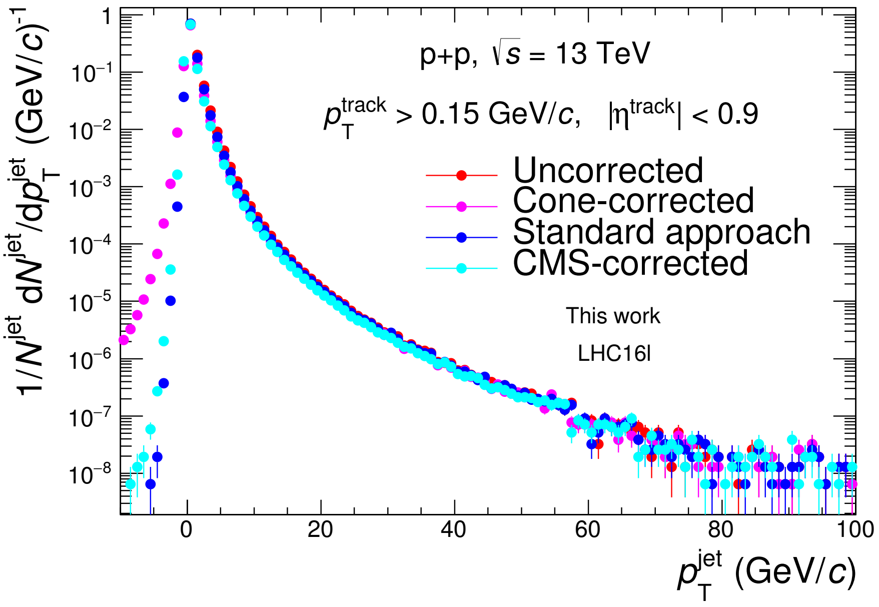

Figure 5.4: The UE density corrected, anti-k_T $R = 0.4$, charged jet spectra in comparison with the uncorrected spectrum. The red markers correspond to the uncorrected jet p_T, the magenta ones to the perpendicular cones correction, the blue ones to the standard area-based approach and the cyan ones to the CMS-improved correction. All spectra are from the *2016l* period.

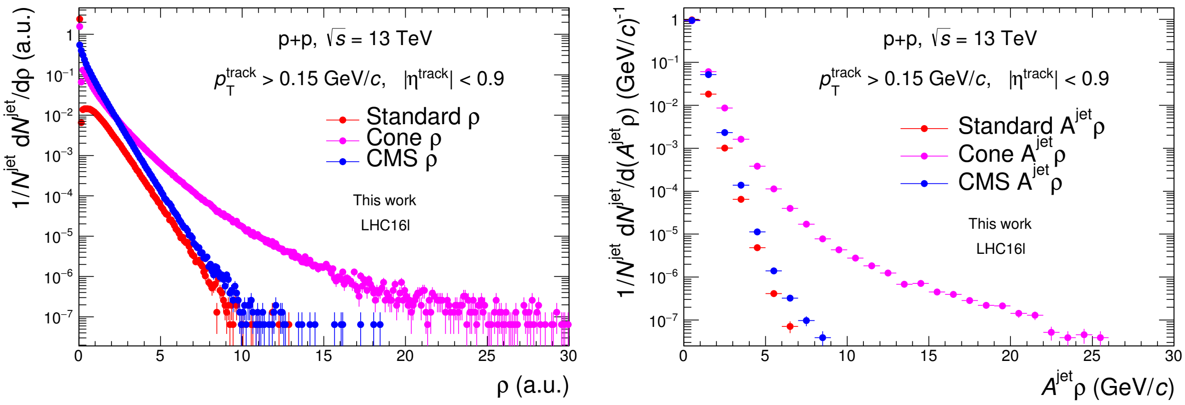

Figure 5.5: **Left:** The underlying event density ρ as calculated with the standard area based approach, CMS method and the perpendicular cones method. **Right:** The p_T correction $A^{\mathrm{jet}}\rho$ as calculated with the standard area based approach, CMS method and the perpendicular cones method. Both quantities are calculated from the *2016l* dataset.

Chapter 6

Unfolding

Raw jet p_{T} spectra measured by a real detector suffer for the inherent flaws of the detector such as the inefficiency of track reconstruction and track momentum smearing. The measured raw jet spectra need to be corrected for these detector effects. In this analysis, these corrections are carried out by *unfolding* based on the singular value decomposition theorem.

The spectrum correction problem can be mathematically formulated as follows. Suppose that the bins of the measured jet p_{T} spectrum are represented by the elements of a vector $\vec{b}$. A linear relation between the original spectrum $\vec{x}$ and the reconstructed p_{T} spectrum $\vec{b}$ is assumed. The detector effects are represented by the *response matrix* $\mathbb{A}$ of the detector. The desired true p_{T} distribution of jets $\vec{x}$ is then obtained by solving the linear system for $\vec{x}$

$$\vec{b} = \mathbb{A}\vec{x}. \tag{6.1}$$

The response matrix $\mathbb{A}$ may be singular and therefore simple inverse matrix may not exist.

6.1 Singular Value Decomposition

To invert the matrix $\mathbb{A}$, an approach based on the singular value theorem [44] is utilised.

Theorem 1 (SVD)**.** *Let* $\mathbb{A} \in \mathbb{R}^{m,n}$ *be an arbitrary matrix where* $n, m \in \mathbb{N}$. *Then* $\mathbb{A}$ *admits a decomposition of the form*

$$\mathbb{A} = \mathbb{U}\mathbb{S}\mathbb{V}^T, \tag{6.2}$$

where $\mathbb{U} \in \mathbb{R}^{m,m}$ *and* $\mathbb{V} \in \mathbb{R}^{n,n}$ *are orthogonal matrices and* $\mathbb{S} = \mathrm{diag}(\mathbb{S}_{11}, \mathbb{S}_{22}, ..., \mathbb{S}_{rr})$. *The numbers* $\mathbb{S}_{11} \geq \mathbb{S}_{22} \geq \mathbb{S}_{rr} \geq 0$ *are called the singular values of* $\mathbb{A}$ *where* $r = \mathrm{rank}(\mathbb{A})$.

The decomposition (6.2) can be interpreted as a rotation represented by the orthogonal matrix $\mathbb{V}^T$ then a scaling by a diagonal matrix $\mathbb{S}$ and finally another rotation by an orthogonal matrix $\mathbb{U}$.

In [44], the problem (6.1) is transformed into minimising the quadratic form

$$(\bar{\mathbb{A}}\vec{y} - \vec{b})(\bar{\mathbb{A}}\vec{y} - \vec{b})^T + \tau\,(\mathbb{C}\vec{y})^T\,\mathbb{C}\vec{y}, \tag{6.3}$$

where the vector $y_i = \frac{x_i}{x_i^{\mathrm{ini}}}$ and the matrix $\bar{\mathbb{A}}_i = \mathbb{A}_{ij} x_j^{\mathrm{ini}}$ are rescaled by an initial estimate of the solution $\vec{x}^{\mathrm{ini}}$—the so-called *prior spectrum.* This scaling is done in order to make the $\vec{y}$ slowly varying (ideally, $\vec{y}$ should be flat). The matrix $\mathbb{C}$ is added in order to regularise the initial problem which may be singular. The final solution is expected to minimally fluctuate around the prior spectrum and therefore the last term in (6.3) represents the measure of oscillations. If the measure of oscillations is represented as the square of second derivatives of $\vec{y}$ then $\mathbb{C}$ is chosen as the matrix of the second differences between subsequent elements of $\vec{y}$. The parameter τ represents the strength of the regularisation. The matrix $\mathbb{C}$ can be expressed as

$$\mathbb{C} = \begin{pmatrix} -1+\varepsilon & 1 & 0 & 0 & \cdots & 0 \\ 1 & -2+\varepsilon & 1 & 0 & \cdots & 0 \\ 0 & 1 & -2+\varepsilon & 1 & \cdots & 0 \\ \vdots & \vdots & \vdots & \vdots & \ddots & \vdots \\ 0 & 0 & 0 & 0 & \cdots & -1+\varepsilon \end{pmatrix}. \tag{6.4}$$

The small increment ε is added to the diagonal in order to make $\mathbb{C}$ invertible. A sensible choice for ε is on the order of $\varepsilon = 10^{-3}$ [44]. The minimisation of (6.3) is searched by the *damped least squares* method from the overdetermined system

$$\begin{pmatrix} \bar{\mathbb{A}}\mathbb{C}^{-1} \\ \sqrt{\tau}\mathbb{I} \end{pmatrix} \mathbb{C}\vec{y} = \begin{pmatrix} \vec{\bar{b}} \\ \vec{0} \end{pmatrix}. \tag{6.5}$$

The SVD is now applied on the matrix $\bar{\mathbb{A}}\mathbb{C}^{-1}$

$$\bar{\mathbb{A}}\mathbb{C}^{-1} = \mathbb{U}\mathbb{S}\mathbb{V}^T. \tag{6.6}$$

The regularised solution of (6.1) can be expressed as

$$\vec{y}^{\tau} = \mathbb{C}^{-1}\mathbb{V}\vec{z}^{\tau}, \tag{6.7}$$

where

$$z_i^{\tau} := \frac{d_i \mathbb{S}_{ii}}{\mathbb{S}_{ii}^2 + \tau}, \tag{6.8}$$

and

$$\vec{d} := \mathbb{U}^T \vec{\bar{b}}. \tag{6.9}$$

The unfolded solution x^{true} is the obtained from y^{τ} by rescaling by the initial prior distribution.

According to [44], the regularisation parameter τ can be determined by plotting $\log|d_i|$ versus i as in Figure 6.1. The regularisation parameter is chosen at the place where statistically significant components of the vector $\vec{d}$ change to randomly oscillating which is

$$\tau = \mathbb{S}_{kk}^2, \tag{6.10}$$

where k is the component indicated by the arrow in Figure 6.1 and $\mathbb{S}_{kk}$ is the $k-$th diagonal element of the matrix $\mathbb{S}$ from SVD. The components of d_i where statistical fluctuations dominate are random numbers following $|N(0,1)|$, where $N(0,1)$ is the normal distribution with mean 0 and standard deviation 1. If $|d_i|$ vs. i is plotted, these components fluctuate around the expectation value $E[|N(0,1)|] = \sqrt{\frac{2}{\pi}}$.

6.2 Response matrix

The response matrix of the detector was obtained from the simulated $\mathrm{p}+\mathrm{p}$, $\sqrt{s} = 13$ TeV PYTHIA 8 events (MC production *2017f8a*) anchored to the period *2016l* and is seen in Figure 6.2.

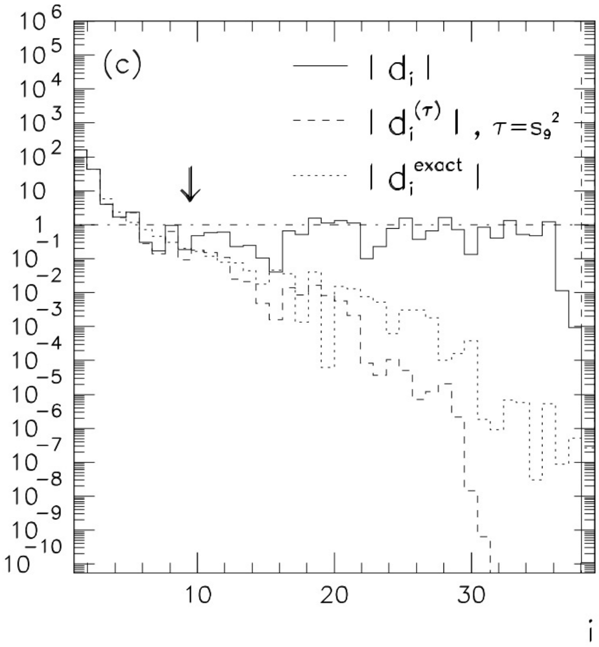

Figure 6.1: Illustration of $\log|d_i|$ versus i for choosing the optimal value for τ. Taken from [44].

In this case, the response matrix represents the relation between the jet p_T at the particle level and the corresponding jet p_T at the detector level. The matching between the corresponding jets at the particle level and at the detector level is done based on their mutual angular distance.

In order to populate the response matrix in high-p_T regions, it has been generated in a PYTHIA regime that allows the transferred 4-momentum in the simulated interaction to be constrained. This is done by setting the PYTHIA parameters *pTHatMin* and *pTHatMax*. The border values for the constrained p_T hard bin are

$$(0, 5, 11, 21, 36, 57, 84, 117, 152, 191, 234, 1000000)\ \mathrm{GeV}/c. \tag{6.11}$$

Constraining the transferred 4-momentum introduces an obvious bias to the response matrix. The individual response matrices for each p_T hard bin are therefore weighted. The weighting coefficient [20] is determined by the cross-section of the given p_T hard bin and the number of trials for each p_T hard interval according to the following equation

$$\left.\frac{\mathrm{d}\sigma_\mathrm{jet}}{\mathrm{d}p_\mathrm{T}^\mathrm{jet}}\right|_\mathrm{MB} = \sum_{p_\mathrm{T}\ \text{hard bin}} \frac{\sigma}{N_\mathrm{trials}} \left.\frac{\mathrm{d}N_\mathrm{jet}}{\mathrm{d}p_\mathrm{T}^\mathrm{jet}}\right|_{p_\mathrm{T}\ \text{hard bin}}, \tag{6.12}$$

where MB labels the minimum bias jet p_T spectrum, σ is the cross-section of the collisions in each p_T hard bin and N_trials is the number of events per the same p_T hard bin. Both σ and N_trials are calculated directly by PYTHIA.

The response matrix has been rebinned according to (5.1) in the reconstructed jet p_T axis and according to

$$p_\mathrm{T,true}^\mathrm{jet} = \{0, 10, 15, 20, 25, 30, 50, 80, 300\}\ (\mathrm{GeV}/c), \tag{6.13}$$

in the true jet p_T axis and is depicted in Figure 6.3.

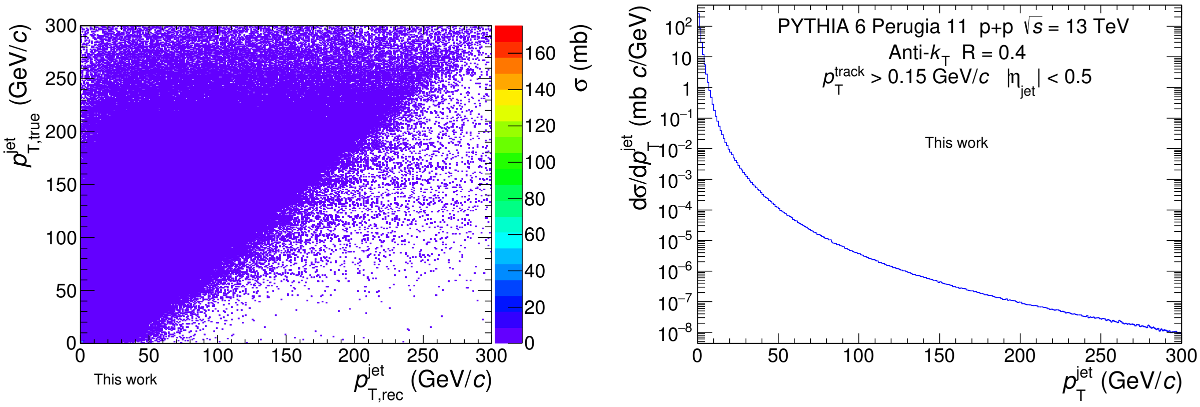

Figure 6.2: **Left:** The response matrix of charged, anti-k_T $R = 0.4$ jets obtained from the Monte Carlo PYTHIA 6 Perugia 11 simulation *2017f8a* anchored to *2016l*. **Right:** The MC generated particle level, inclusive, charged, anti-k_T $R = 0.4$ jet p_T spectrum corresponding to the response matrix.

6.3 Results

For a simple cross-check, the SVD unfolded p_T spectra will be compared with the spectrum corrected by a bin-by-bin correction. A bin-by-bin correction is the simplest method of jet spectra correction. Each bin of the p_T spectrum is corrected as

$$B = \frac{T^{\mathrm{MC}}}{R^{\mathrm{MC}}} \cdot R^{\mathrm{data}}, \tag{6.14}$$

where B is the bin content of the corrected spectrum, T^{MC} is the bin content of the true spectrum obtained from Monte Carlo, R^{MC} is the bin content of the Monte Carlo reconstructed spectrum and R^{data} is the bin content of the raw spectrum.

The SVD-unfolded and raw jet p_T spectra from the period *2016l* are compared in Figure 6.5. The unfolding has been done with the response matrix shown in Figure 6.3. The prior distribution was generated using a minimum bias, PYTHIA 8 tune 4C, $\mathrm{p+p}$ events at $\sqrt{s} =$ 13 TeV and is shown in Figure 6.4. The d_i distribution of the SVD unfolding is presented in Figure 6.7. The regularisation parameter $k = 6$ has been chosen. In order to check the consistency of the unfolding, the unfolded spectrum is convoluted with the response matrix. This *folded* spectrum is then compared with the raw spectrum. The comparison of the raw and folded jet p_T spectra is illustrated in Figure 6.6. The folded and raw spectrum may not coincide perfectly because the SVD unfolding procedure also involves a smoothening i.e. it suppresses fluctuations. Therefore the ratios of the folded spectrum for several values of the regularisation parameter to the raw spectrum are also drawn in Figure 6.7 . The ratio is plotted together with a grey band which shows the relative statistical errors of the raw spectrum in order to assess to what extent are the differences caused by the fluctuations of the input data. The simple bin-by-bin correction does not include such a regularisation procedure.

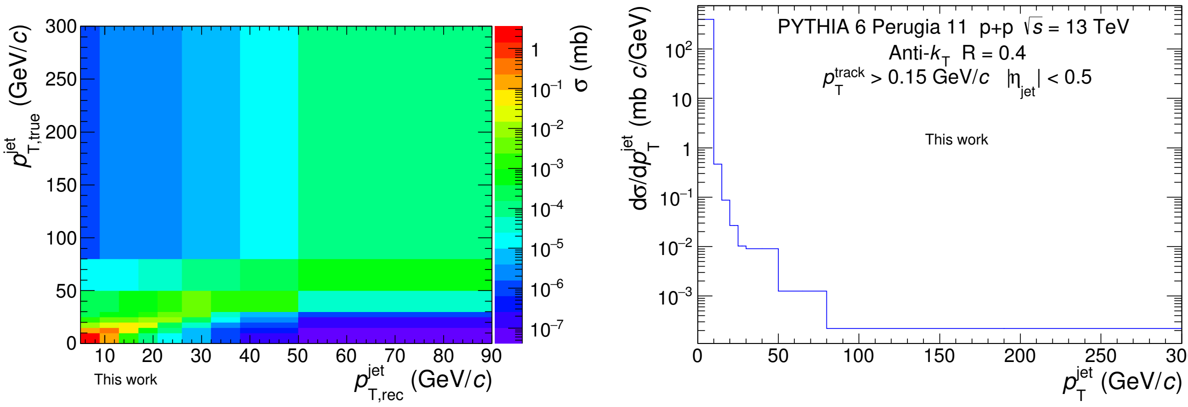

Figure 6.3: **Left:** The response matrix of charged, anti-k_T $R = 0.4$ jets obtained from the Monte Carlo PYTHIA 6 Perugia 11 simulation *2017f8a* anchored to *2016l*. The response matrix is rebinned according to (5.1) and (6.13). **Right:** The MC generated true inclusive, charged, anti-k_T $R = 0.4$ jet p_T spectrum corresponding to the response matrix. The jet spectrum is rebinned according to (6.13).

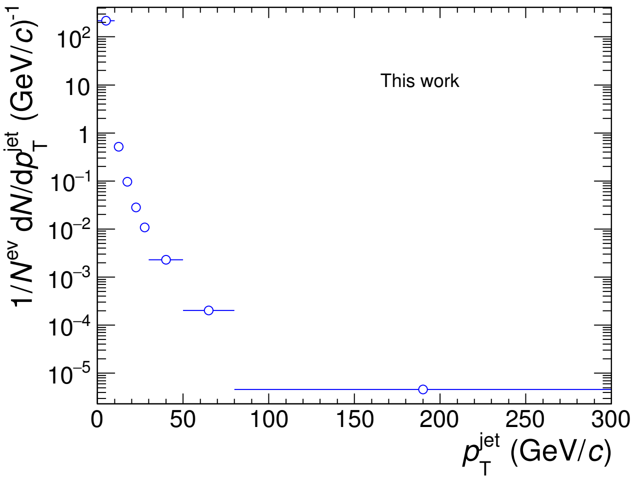

Figure 6.4: An inclusive p_T spectrum of charged, anti-k_T $R = 0.4$ jets from $\mathrm{p+p}$ collisions at $\sqrt{s} = 13$ TeV as generated by PYTHIA 8 tune $4C$. This spectrum is used as a prior for the unfolding.

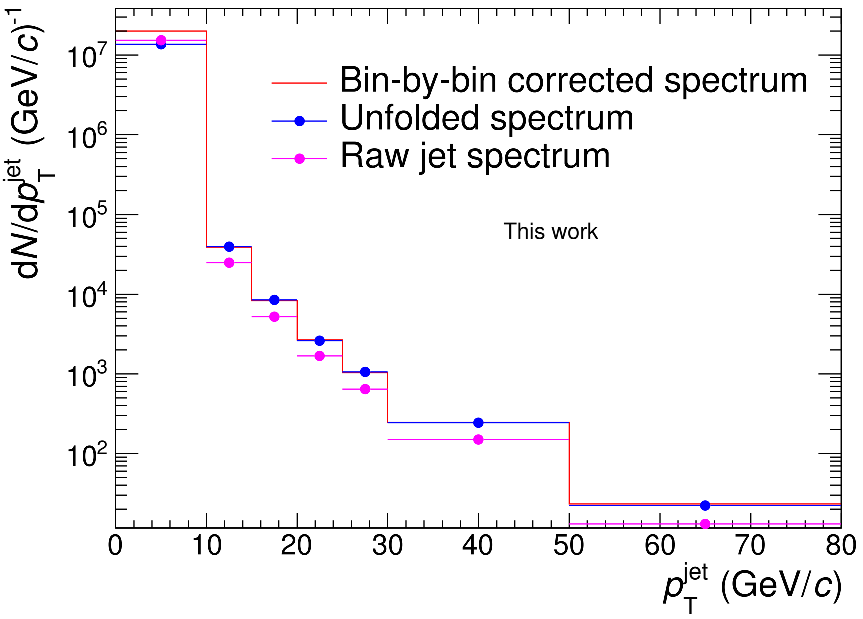

Figure 6.5: The comparison of the inclusive, charged, raw jet p_T spectrum in blue, the bin-by-bin correction in red and the SVD-unfolded jet p_T spectrum in green. The bin-by-bin correction has been done according to (6.14).

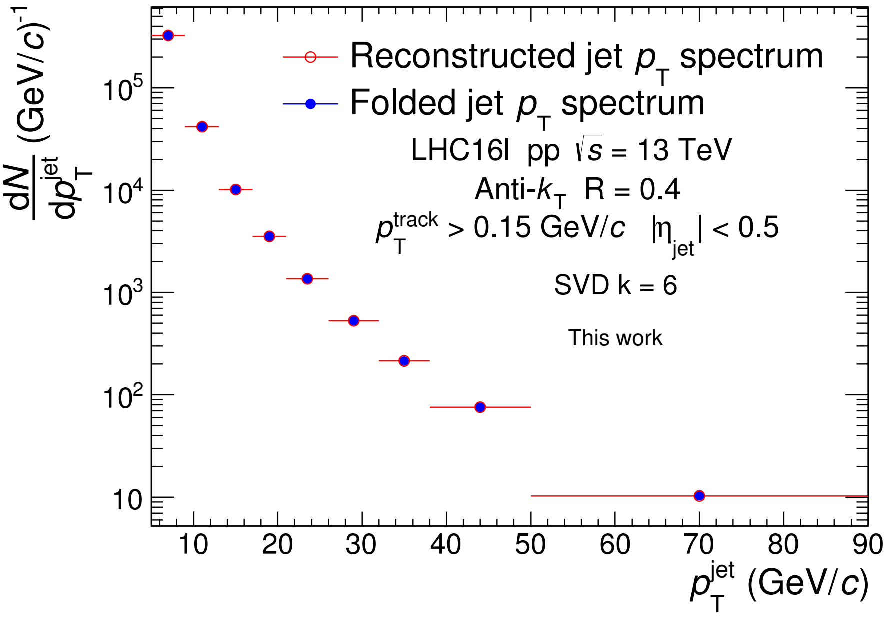

Figure 6.6: The comparison of the folded and raw jet p_T spectra.

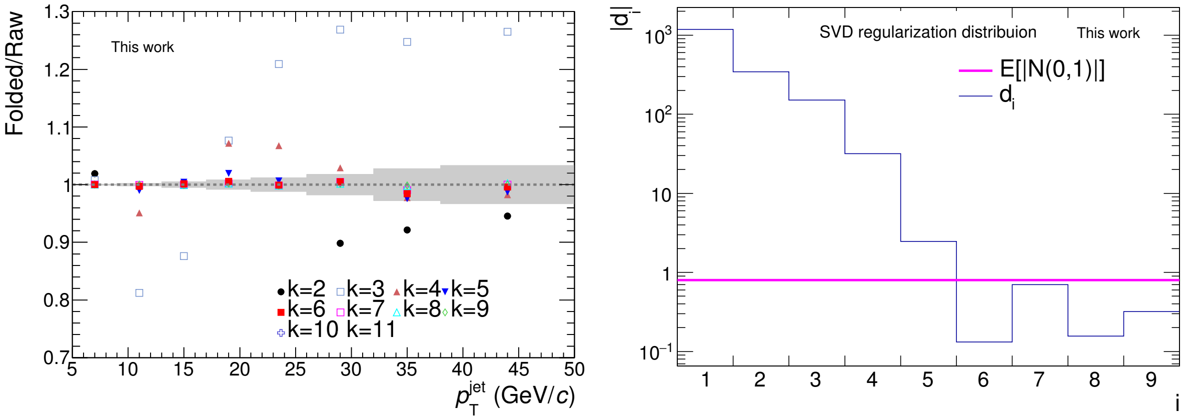

Figure 6.7: **Left:** The ratio of the folded and raw jet p_{T} spectra for several values of the SVD regularisation parameters. The grey band represents the mean statistical errors of the raw jet p_{T} spectrum. **Right:** The d_i distribution of the SVD unfolding. The magenta line represents the expectation value $E[|N(0,1)|]$ of the absolute value of the normal distribution with 0 mean and a standard deviation of 1. $k = 6$ has been chosen as the regularisation parameter.

6.4 Closure test

In order to check the consistency of the response matrix and the whole correction procedure an independent Monte Carlo spectrum is unfolded. The detector level inclusive p_{T} spectrum of charged anti-k_{T} $R = 0.4$ jets from $\mathrm{p+p}$ collisions at $\sqrt{s} = 13$ TeV calculated by Perugia 11 PYTHIA production *2016j2a2* anchored to *2016l* was unfolded using the response matrix shown in Figure 6.2 and compared with the corresponding particle level jet spectrum. The response matrix and the tested spectrum are statistically independent. The prior spectrum for the unfolding has been generated as minimum bias, charged, anti-k_{T} $R = 0.4$ jet spectrum from $\mathrm{p+p}$ collisions at $\sqrt{s} = 13$ TeV using PYTHIA 8, tune $4C$ and is shown in Figure 6.8. The regularisation distribution and the ratio of the raw and folded spectra are shown in Figure 6.9. Parameter $k = 6$ has been chosen.

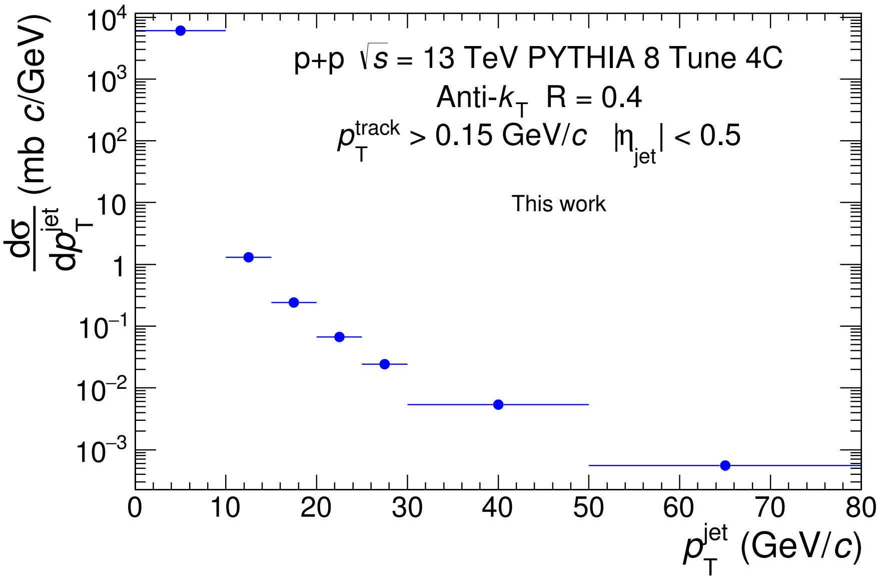

Figure 6.8: The prior spectrum used for the closure test obtained from minimum bias $\mathrm{p+p}$ collisions at $\sqrt{s} = 13$ TeV simulated by PYTHIA 8, tune $4C$.

The comparison of the true and unfolded spectra is shown in Figure 6.10. The consistency check shows a good agreement between the true and unfolded spectra in the range above 15 GeV/c which is the region of interest and thus validates the unfolding procedure.

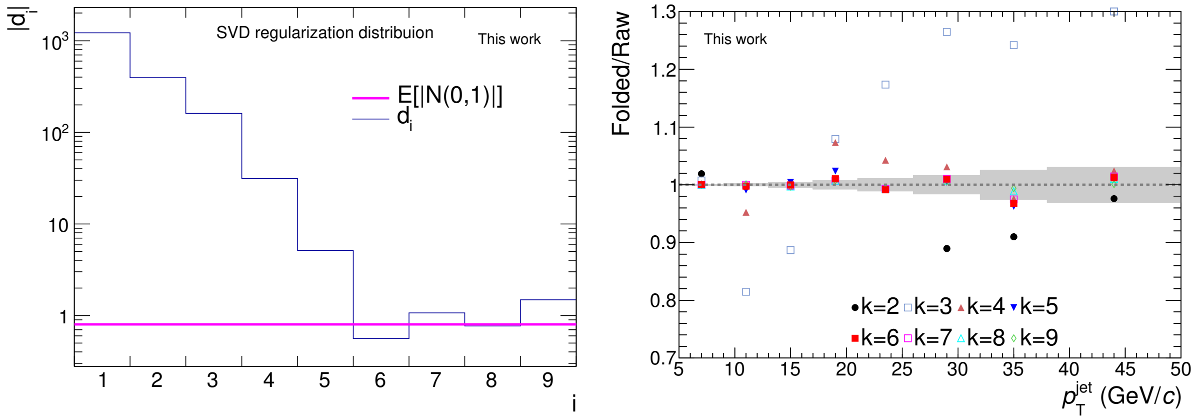

Figure 6.9: **Left:** The SVD regularisation distribution of the closure test. **Right:** The ratio of the raw and folded spectra for the closure test. The grey band represents the size of the relative statistical error of the input raw spectrum.

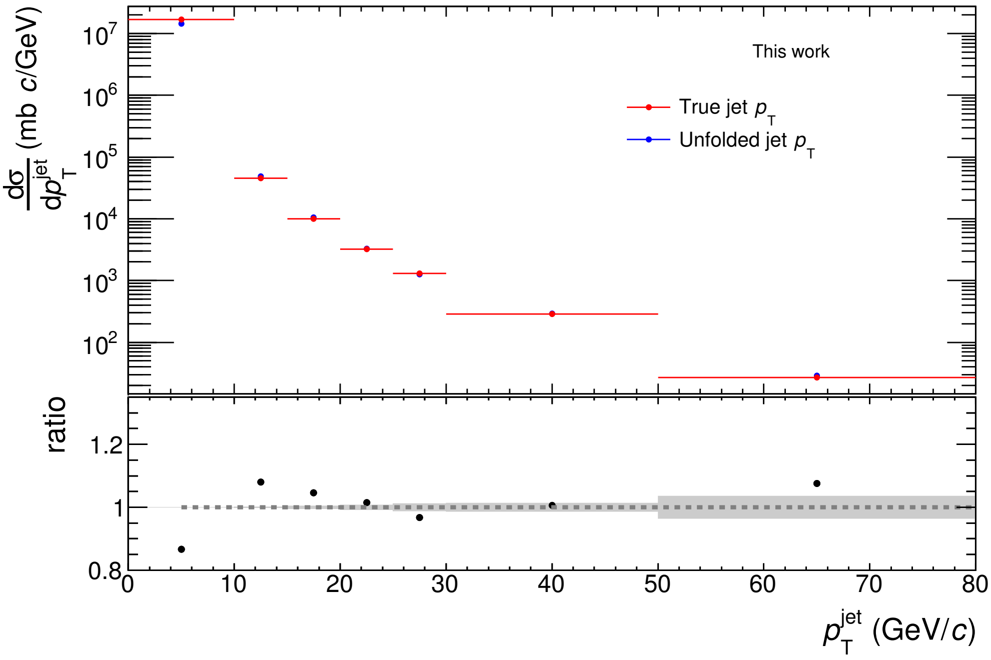

Figure 6.10: Closure test of the unfolding procedure. **Upper panel:** The true and unfolded charged, anti-k_T $R = 0.4$ spectra of jets from $\mathrm{p+p}$ collisions at $\sqrt{s} = 13$ TeV of the Monte Carlo production *2016j2a2*. **Lower panel:** The ratio of the true and unfolded spectra. The statistical errors of the ratio are not drawn due to a strong correlation of the spectra. The grey band represents the relative statistical uncertainty of the true spectrum.

Chapter 7

Systematic uncertainties

This section explores the dependency of the fully corrected spectra on the parameters of the analysis by estimating systematic uncertainties. The following sources of systematic uncertainties have been considered:

1. the choice of the unfolding algorithm (SVD or Bayesian) and of regularisation parameter,
2. the choice of the prior spectrum,
3. the choice of the binning and range of the raw spectrum,
4. the track reconstruction efficiency,
5. the transverse momentum resolution.

In order to suppress the influence of statistical uncertainties in the input data on the estimation of the systematic uncertainties the following approach is employed. The systematic uncertainty has been estimated using new p_{T} spectra obtained by randomisation of the measured raw spectrum. The value for each bin of the new spectrum is generated according to the Gaussian distribution with the mean mean set to the original value and the standard deviation set to its statistical error. If the resulting number of counts in a given p_{T} bin is negative the random number is generated again until the bin content is positive. The error is set to the error of the original value. Nineteen new p_{T} spectra have been generated in this manner. Each of these newly generated spectra have been analysed with the primary analysis (PA) settings used above and the modified settings. By considering the median of the ratio of the spectrum obtained with the modified analysis settings and with the PA analysis settings one suppresses the statistical influence on the uncertainties and is left with the systematic uncertainty.

7.1 Unfolding algorithm and regularisation parameter

Bayesian unfolding [45], as implemented in the RooUnfold package [46], is considered as an alternative to the SVD unfolding. The Pearson coefficients of the Bayesian unfolding determine the bin correlations in the unfolded spectrum. The optimal number of iterations is determined according to the convergence of the ratio of the folded and raw spectra shown in Figure 7.2 and the resulting spectrum should have its Pearson coefficients close to a diagonal matrix. The Pearson coefficients for all the iterations are shown in Figure 7.1. The optimal number of

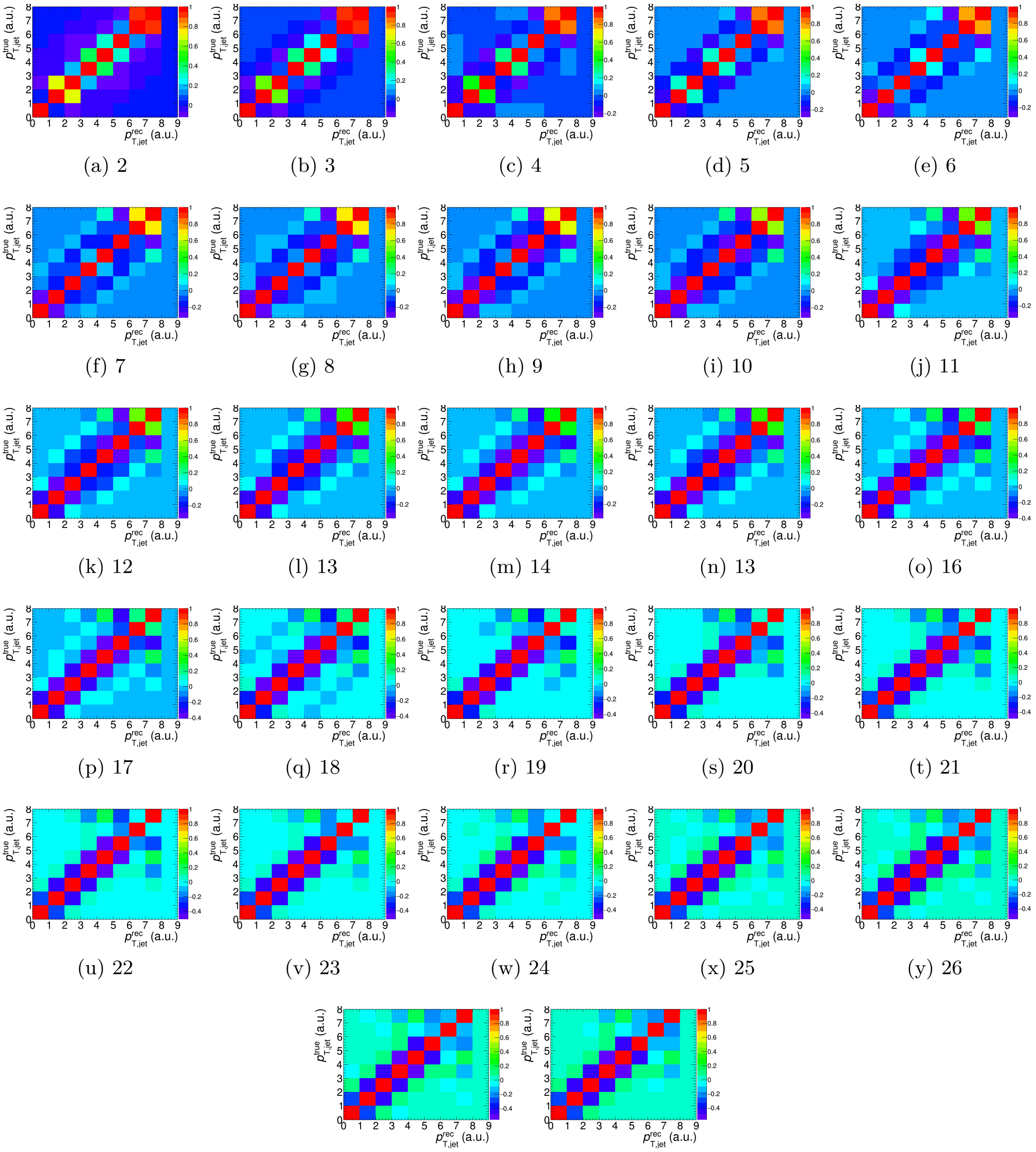

(a) 2 (b) 3 (c) 4 (d) 5 (e) 6

(f) 7 (g) 8 (h) 9 (i) 10 (j) 11

(k) 12 (l) 13 (m) 14 (n) 13 (o) 16

(p) 17 (q) 18 (r) 19 (s) 20 (t) 21

(u) 22 (v) 23 (w) 24 (x) 25 (y) 26

(z) 27 (aa) 28

Figure 7.1: Pearson coefficients for the Bayesian unfolding for the given number of iterations.

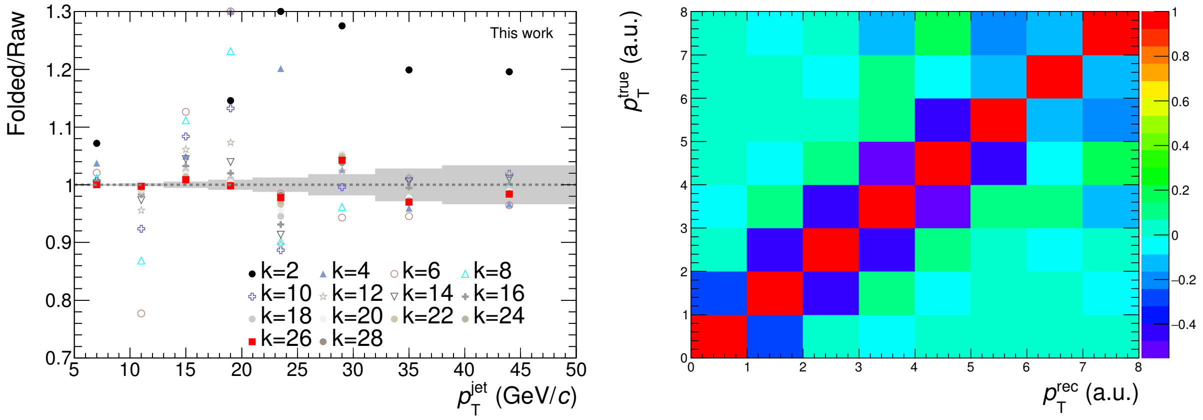

Figure 7.2: **Left:** The ratio of the folded and raw spectra for various iterations of the Bayesian unfolding. The grey band represents the relative statistical error of the raw spectrum. **Right:** The Pearson coefficients for the 26th iteration. The X axis represents the consecutive number of the given p_{T} bin.

iterations has been chosen as 26 and its Pearson coefficients are seen in the right panel of Figure 7.2.

To estimate the influence of the choice of the regularisation parameter in the SVD and Bayesian algorithms the regularisation parameter and the number of iterations have been varied by ±2. The resulting rations of the unfolded spectra obtained with the modified analysis and the PA analysis settings are shown in Figure 7.3.

7.2 Choice of the prior spectrum

Three different prior spectra have been used to determine the systematic uncertainty from the choice of the prior spectrum, namely a minimum bias, particle level p_{T} spectrum of jets in collisions at $\sqrt{s} = 13$ TeV generated by PYTHIA 8 tune $4C$ and a fitted prior spectrum. The priror spectrum used in the PA is generated using hard bins. A smooth spectrum is obtained by fitting the prior spectrum by an exponential at low p_{T} and by a Kaplan function at high p_{T}. The resulting fitted function is

$$A\left(\frac{2}{\pi}\arctan(B(p_{\mathrm{T}}-10))+1\right)\left(1+Cp_{\mathrm{T}}^{2}\right)^{-D} - E\arctan(B(p_{\mathrm{T}}-10))e^{-Fp_{\mathrm{T}}}, \tag{7.1}$$

where A, B, C, D, E and F are fit parameters shown in Table 7.1 and the p_{T} is in GeV/c.

Parameter	Value	Error
A	150	±1
B	0.0277	±0.0003
C	0.0481	±0.0002
D	2.6936	±0.0005
E	9290	±87
F	−1.202	±0.001

Table 7.1: Fit parameters from the prior fit.

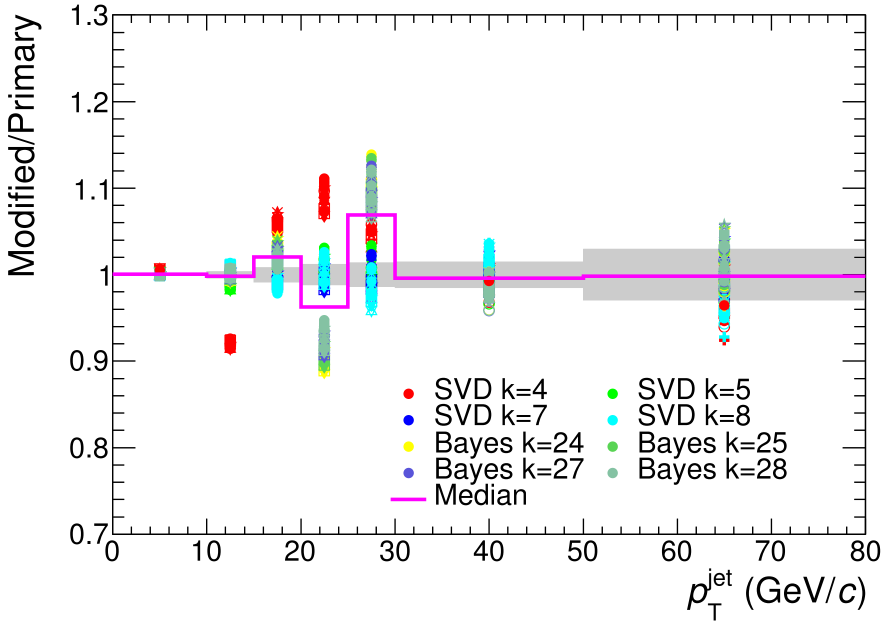

Figure 7.3: The systematic uncertainty due to the choice of the regularisation parameter. The grey band represents the relative statistical uncertainties of the unfolded spectra.

The estimated uncertainties from the choice of the prior spectrum are depicted in Figure 7.4.

7.3 Binning

Two different binnings have been used to estimate the susceptibility of the unfolded solution to the choice of the binning. They are referred to as *Binning B* and *Binning C* where the original PA analysis binning is *Binning A*

$$\text{Binning A} : 5, 9, 13, 17, 21, 26, 32, 38, 50, 90 (\text{GeV}/c), \tag{7.2a}$$

$$\text{Binning B} : 5, 8, 12, 16, 29, 24, 29, 35, 45, 110 (\text{GeV}/c), \tag{7.2b}$$

$$\text{Binning C} : 5, 10, 14, 18, 23, 28, 35, 41, 55, 100 (\text{GeV}/c). \tag{7.2c}$$

The systematic uncertainty due to the choice of the binning of the raw spectrum is depicted in Figure 7.5.

7.4 Track reconstruction efficiency

The systematic uncertainties caused by the inefficiency of the reconstruction of charged tracks is investigated according to [47]. The uncertainty of the track reconstruction efficiency is assessed to be 4 % [47] and a new response matrix is generated by randomly removing 4 % of the tracks. The raw spectrum is then unfolded with this modified response matrix and compared to the primary analysis. The systematic uncertainties of the track reconstruction efficiency are shown in Figure 7.6. The track reconstruction efficiency is the highest contributor to the systematic uncertainties with a value of approximately 10%.

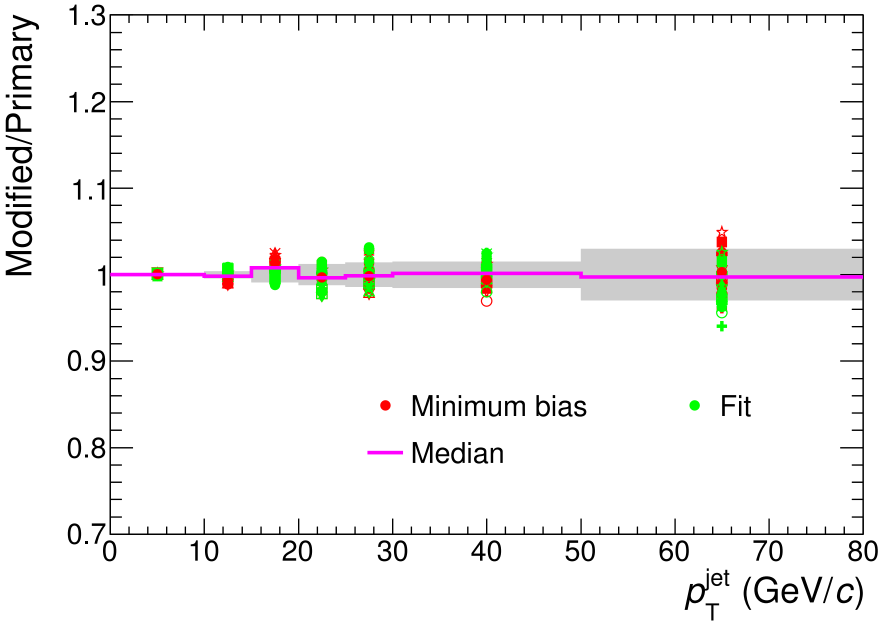

Figure 7.4: The systematic uncertainties due to the choice of the prior spectrum. The grey band represents the relative statistical uncertainties of the unfolded spectra.

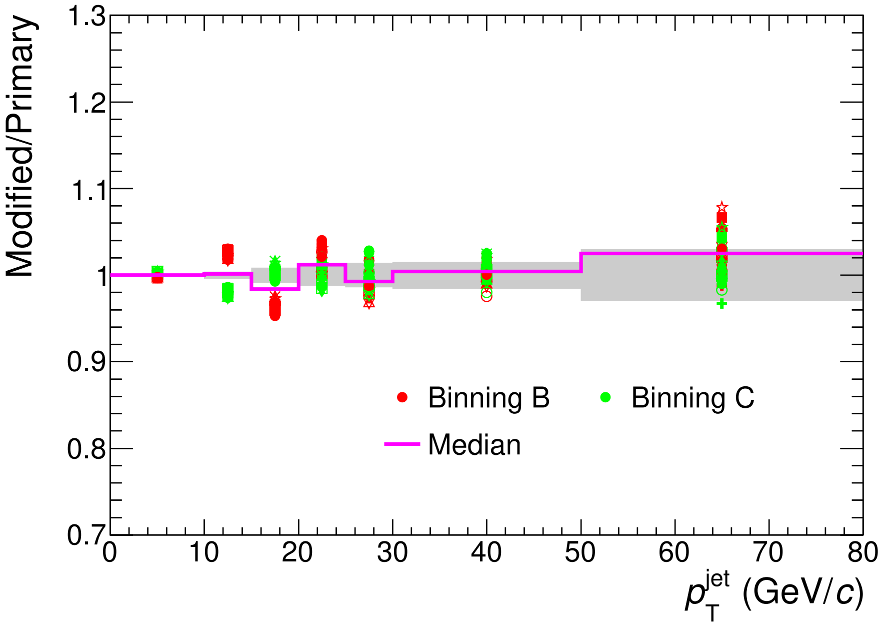

Figure 7.5: The systematic uncertainty due to the choice of the binning of the raw spectrum according to (7.2). The grey band represents the relative statistical uncertainties of the unfolded spectra.

7.5 Momentum smearing

The parameters of the track p_{T} smearing have been obtained from the covariance matrix of the tracking in real data. The track p_{T} smearing is determined from the $\frac{\sigma_{1/p_{\mathrm{T}}}}{1/p_{\mathrm{T}}}$ versus p_{T}

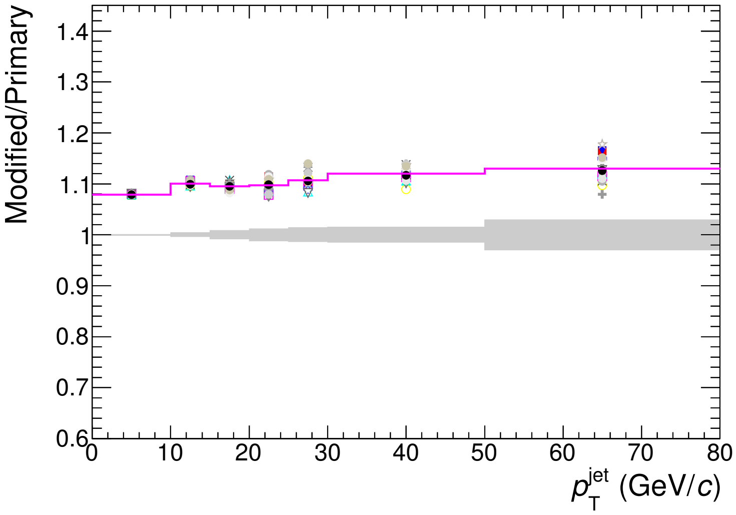

Figure 7.6: The systematic uncertainty due to the track reconstruction efficiency. The grey band represents the relative statistical errors of the unfolded spectrum.

distribution (shown in Figure 7.7). The mean value of each bin of $\frac{\sigma_{1/p_{\mathrm{T}}}}{1/p_{\mathrm{T}}}$ as a function of track p_{T} is parameterised by

$$\alpha + \beta\sqrt{1/p_{\mathrm{T}} + \gamma}, \tag{7.3}$$

where α, β and γ are fit parameters. For low p_{T} values (under 10 GeV/c) instead of the fit, the mean values in each p_{T} bin are used to determine the smearing. The mean value of $\frac{\sigma_{1/p_{\mathrm{T}}}}{1/p_{\mathrm{T}}}$ is shown in Figure 7.8 and the parameters of the corresponding fit are given in Table 7.2.

The estimation of the systematic uncertainties due to track p_{T} smearing follows the procedure described in [48] and the accompanying analysis note. The systematic uncertainty is estimated from a shift of the $1/p_{\mathrm{T}}$ spectra of positively and negatively charged particles. The $1/p_{\mathrm{T}}$ spectra of negatively and positively charged particles were obtained for 50 sections in azimuth. The power law function

$$y(1/p_{\mathrm{T}}) = A(1/p_{\mathrm{T}} - B)^{-n}, \tag{7.4}$$

has been used to fit the $1/p_{\mathrm{T}}$ spectra in the p_{T} range $4-33$ GeV/c. A sample of the fits is shown in Figure 7.9. The fit parameter B corresponds to the shift for a given azimuthal bin configuration. The assumption that B is independent of $1/p_{\mathrm{T}}$ is made. The Root Mean Square (RMS) of B represents the systematic uncertainty of the momentum resolution parameter $\sigma_{1/p_{\mathrm{T}}}$ which is obtained from the covariance matrix of the tracking. The B parameters for positive, negative and combined tracks are shown in Figure 7.10. The RMS of the B parameter values is 0.0127 (0.0126) GeV^{-1} for negatively (positively) charged particles.

The systematic uncertainty of the jet p_{T} smearing was extracted by means of a toy MC simulation. p + p collisions at $\sqrt{s} = 13$ TeV have been simulated with PYTHIA 8, tune 4C. The generated tracks were filtered according to the track reconstruction efficiency seen in Figure 3.3.

The tracks generated in the toy MC model are then duplicated. The smearing $\sigma_{1/p_{\mathrm{T}}}$ is calculated according to the fit. One set is smeared according to $\sigma_{1/p_{\mathrm{T}}}$ and another according to $\sigma_{1/p_{\mathrm{T}}} + \mathrm{RMS}_B$. Thus the smearing $\sigma_{1/p_{\mathrm{T}}}$ is now modified by adding the RMS value of B (p_{T} in GeV/c)

$$\sigma_{1/p_{\mathrm{T}}} = \left(-0.36 + 0.0194\sqrt{360 + 1/p_{\mathrm{T}}}\right) 1/p_{\mathrm{T}} + 0.0127. \tag{7.5}$$

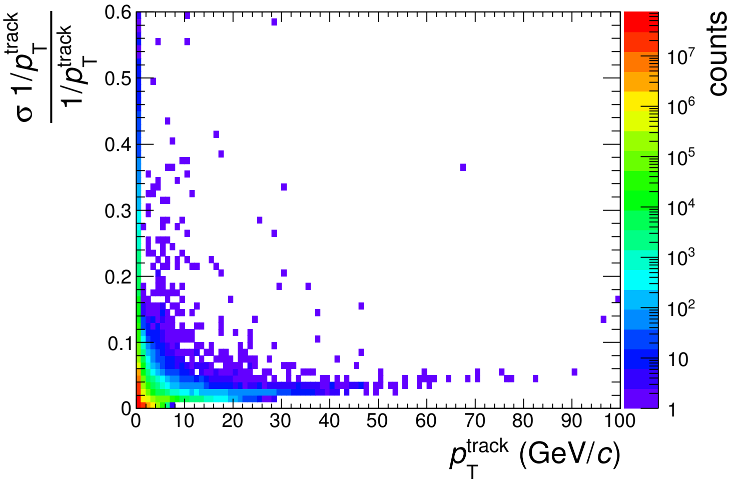

Figure 7.7: The $\frac{\sigma_{1/p_\mathrm{T}}}{1/p_\mathrm{T}}$ as a function of track p_T.

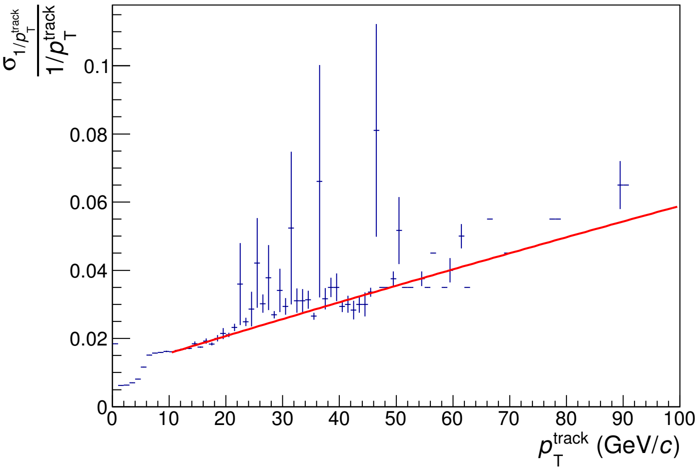

Figure 7.8: The mean of the azimuthal smearing $\frac{\sigma_{1/p_\mathrm{T}}}{1/p_\mathrm{T}}$ vs. track p_T obtained from the track covariance matrix with its fit (7.3).

Parameter	Value	Error
α	-0.36	± 0.03
β	0.0194	± 0.0008
γ	360	± 30

Table 7.2: The $\frac{\sigma_{1/p_\mathrm{T}}}{1/p_\mathrm{T}}$ fit parameters.

Then jets are searched in the true and both reconstructed track sets. True and reconstructed jets are matched by minimising the angular distance between each pair of jets. The resulting response matrices are drawn in Figure 7.11.

The raw spectra were unfolded using both matrices. The smearing with σ_{1/p_T} has been taken

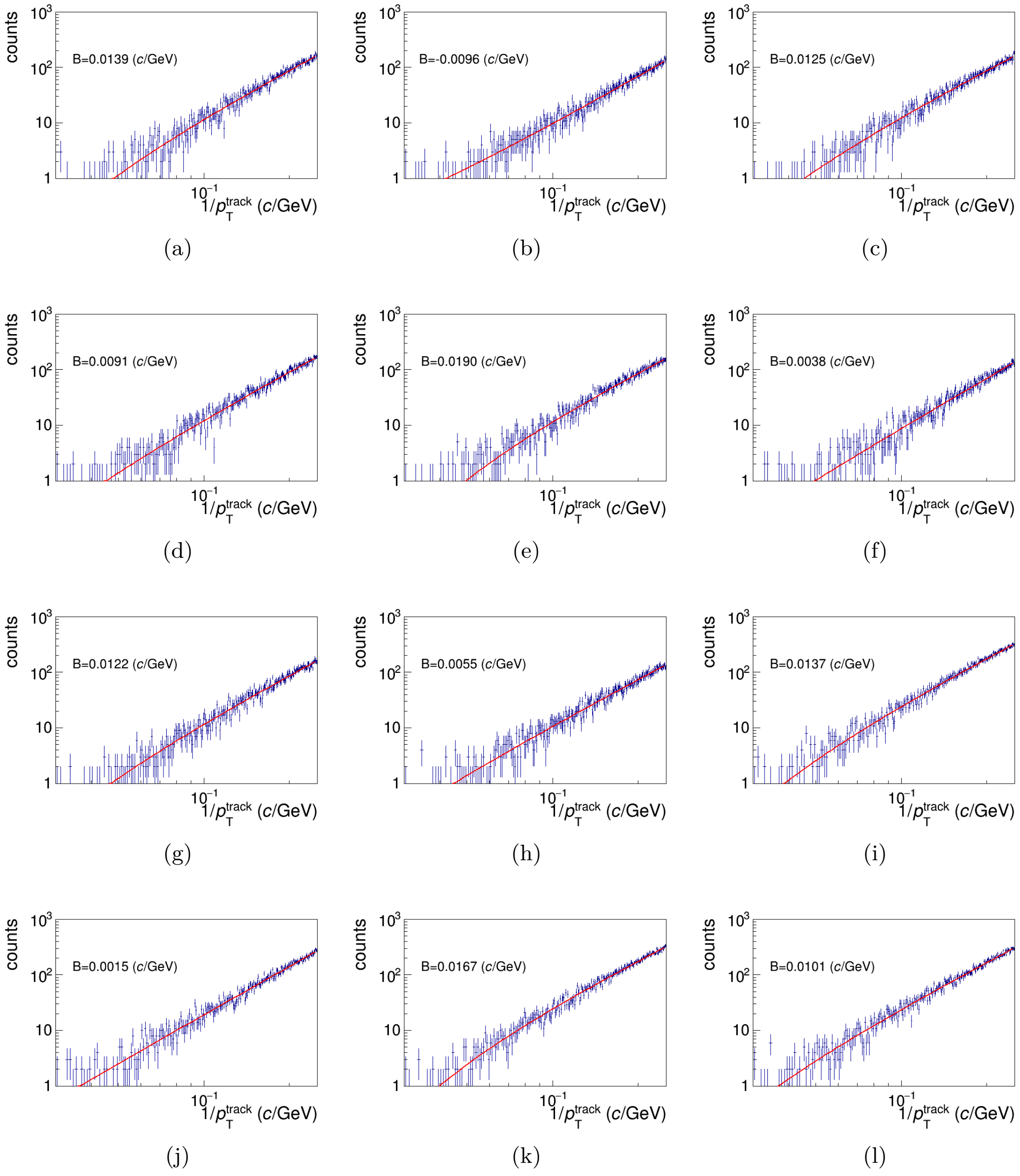

(a) (b) (c)

(d) (e) (f)

(g) (h) (i)

(j) (k) (l)

Figure 7.9: A sample of the fits of $1/p_{\mathrm{T}}$ spectra with (7.4). $(a)-(d)$ corresponds to negative tracks in the 9th, 19th, 29th and 39th bins in azimuth respectively, $(e)-(h)$ to positive tracks in the 9th, 19th, 29th and 39th bins in azimuth respectively and $(i)-(l)$ to all tracks in the 9th, 19th, 29th and 39th bins in azimuth respectively.

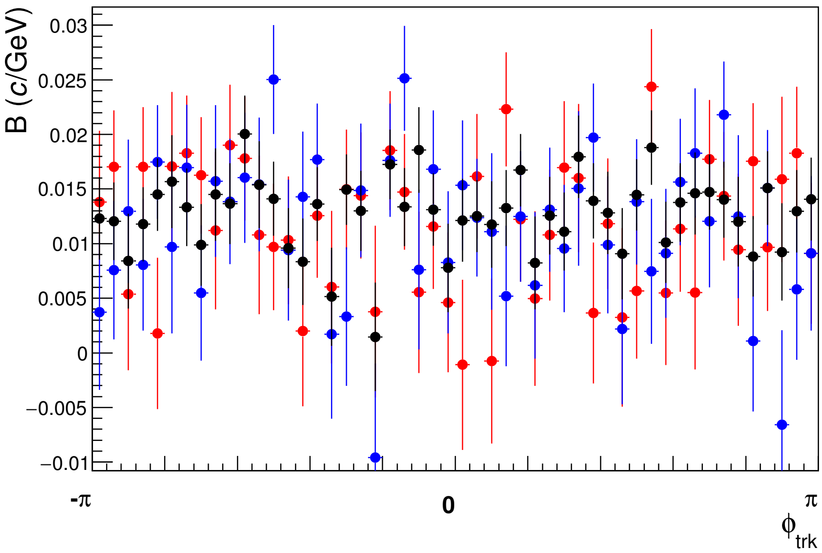

Figure 7.10: The B parameters of the fit as a function of the azimuth. The red and blue points correspond to positively and negatively charged tracks respectively whereas black points are combined tracks.

as the PA settings and the modified settings was smeared by $\sigma_{1/p_{\mathrm{T}}} + \mathrm{RMS}_B$. The estimation of the systematic uncertainties has been carried out in a similar manner to the previous chapters. The ratios of the modified and primary settings together with the median representing the systematic uncertainty are shown in Figure 7.12.

7.6 Total systematic uncertainties

The systematic uncertainties from each source are assumed to be symmetrical and have been combined in quadrature. The resulting total systematic uncertainties are depicted in Figure 7.13.

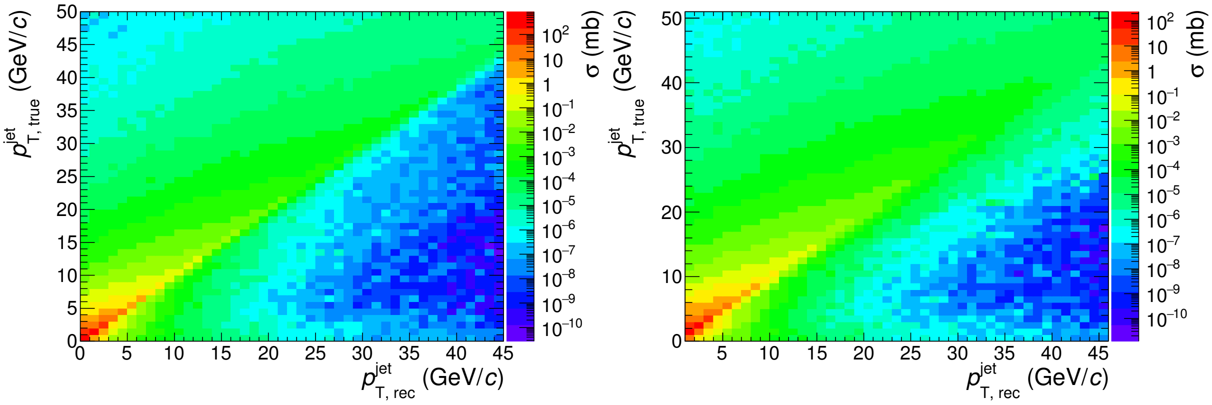

Figure 7.11: **Left:** The response matrix of inclusive, charged anti-k_{T} $R = 0.4$ jets resulting from the tracks smeared according to $\sigma_{1/p_{\mathrm{T}}}$. **Right:** The response matrix of inclusive, charged anti-k_{T} $R = 0.4$ jets resulting from the tracks smeared according to $\sigma_{1/p_{\mathrm{T}}} + \mathrm{RMS}_B$.

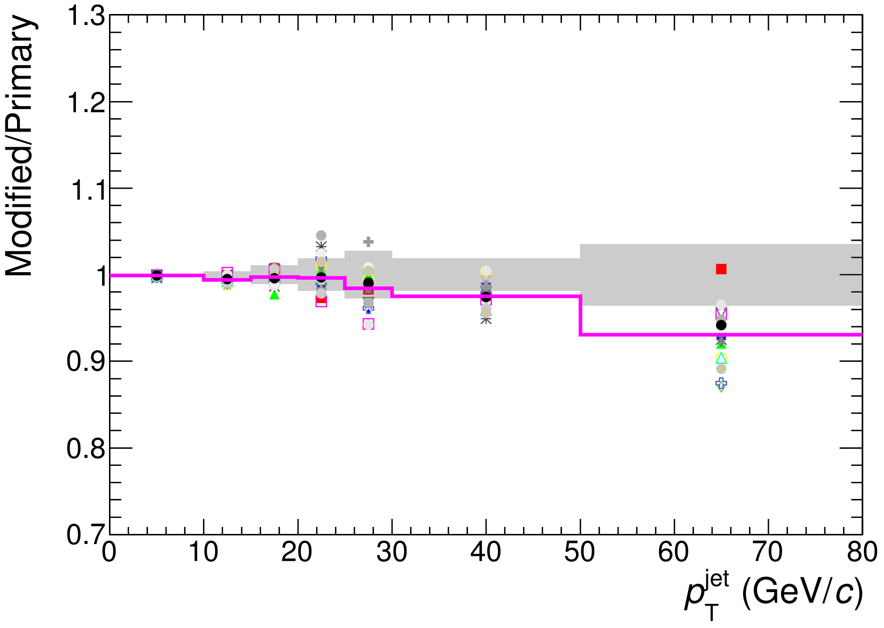

Figure 7.12: The systematic uncertainty due to the smearing of p_{T}. The grey band represents the relative statistical uncertainties of the unfolded spectra.

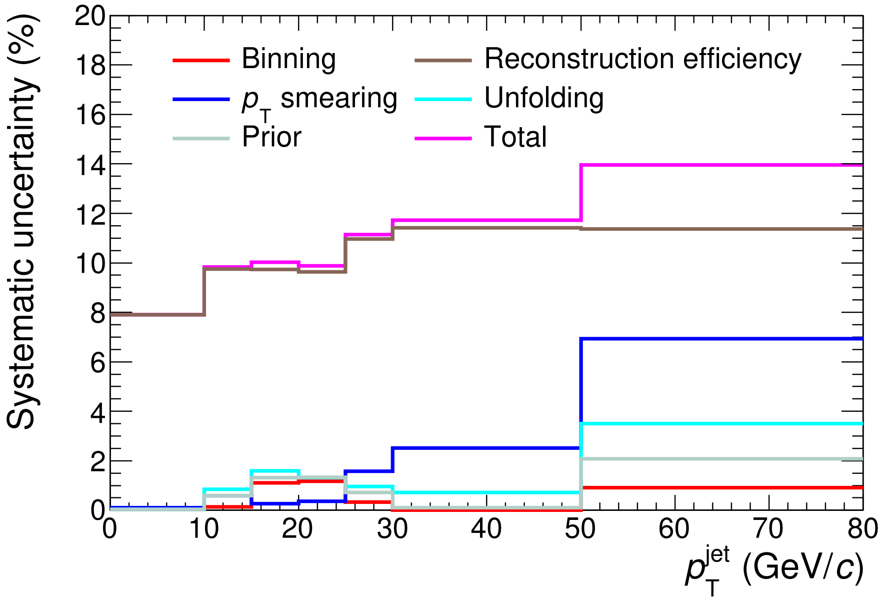

Figure 7.13: The estimated systematic uncertainties from different sources and the resulting total systematic uncertainty.

Chapter 8

Comparison of the final spectrum to the predictions of MC generators

The inclusive, charged, anti-k_T $R = 0.4$ jet p_T spectrum obtained in the previous chapters through unfolding is shown in Figure 8.1. The spectra were normalised per event and scaled by the cross-section of the *V0AND* trigger ($\sigma_{V0AND} = 57.13$ mb [49]). The measured spectra are then compared with particle-level spectra calculated by two MC generators. The first generator is PYTHIA 8 tune $4C$ [20]. The second MC generator considered is JEWEL [50] version 2.2.0. JEWEL is a MC generator used in simulating jet propagation through QGP. Here, JEWEL is run in a mode where jets are produced in vacuum. JEWEL is based on PYTHIA 6 [51]. In order to populate the spectra in high p_T regions, both MC generators calculated the spectra in the hard bin regime similarly to the procedure used to generate the response matrix mentioned in Chapter 6.

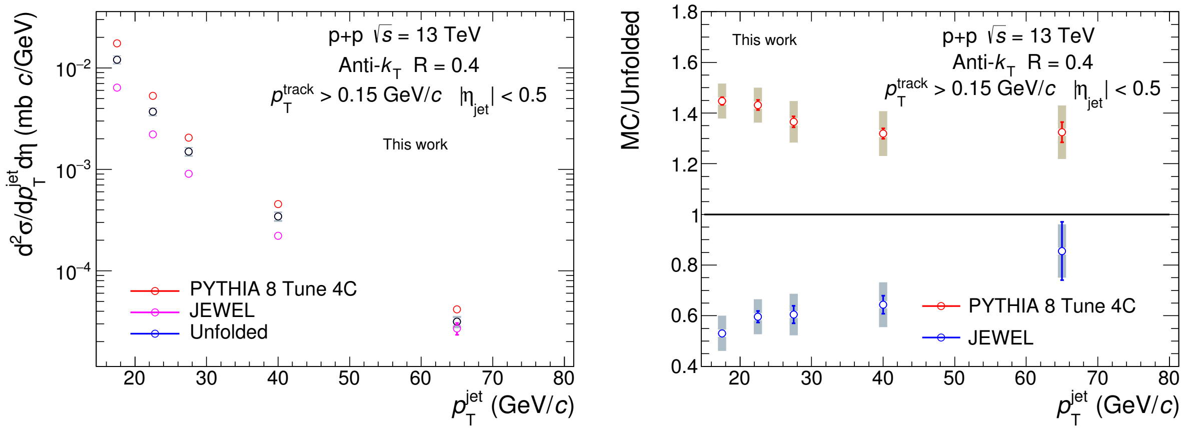

Figure 8.1: **Left:** The comparison of the unfolded inclusive p_{T} spectrum of charged, anti-k_{T} $R = 0.4$ jets with the MC spectra from PYTHIA 8 Tune 4C and JEWEL version 2.2.0. **Right:** The ratio of the unfolded and MC spectra. The colour boxes represent the systematic uncertainties of the unfolded spectrum.

Conclusion

Jets play a key role in many analyses done in high energy physics. Jets in this framework are defined as phenomenological objects by a clusterisation algorithm used to search for high energy particle showers in a collision event. In order to have a compatible description of jets in an experiment and in QCD, jet algorithms have to be collinear and infrared safe. In this we discuss the properties of the two most frequently used jet algorithms—the k_{T} and the anti-k_{T}. The production of high energy particle showers originating in hard processes are commonly accompanied by low energy, soft particles which, from the perspective of this thesis, are considered as background. The possibilities of correcting the high p_{T} spectra for this background are put forth.

This thesis deals with the analysis of inclusive charged, anti-k_{T} jets with $R = 0.4$ produced in p+p collisions at $\sqrt{s} = 13$ TeV. The data were collected by the ALICE experiment. Two datasets were analysed, namely the *2016l* and *2015f*. The latter being rejected due to the inadequate quality of the data. The jet raw spectra were corrected for detector effects by means of SVD unfolding. The jet response matrix was obtained from a detailed, GEANT3-based simulation of ALICE detector response. The whole procedure has been checked by a closure test where an inclusive, charged, anti-k_{T} $R = 0.4$ jet p_{T} spectrum obtained from a Monte Carlo simulation was unfolded using a statistically independent response matrix. The test successfully validated the procedure.

A first estimate of the systematic uncertainties, which reflect the susceptibility of the obtained spectra to modified analysis settings, was made. This has been done by varying certain parameters of the primary analysis. A random smearing of the data was employed in order to eliminate statistical influences on the systematic uncertainties. The following sources of systematic uncertainties were considered: the choice of the unfolding algorithm and its regularisation parameter, the choice of the prior spectrum for the unfolding, the choice of the binning of the raw spectrum, the track reconstruction efficiency and the p_{T} resolution. The largest source of systematic uncertainties is the track reconstruction efficiency—approximately 10 %. The total systematic uncertainty has been determined to be less than 14 %.

The fully corrected jet spectrum was expressed in terms of a cross-section and compared to particle level jet spectra calculated by two MC generators, PYTHIA 8 Tune $4C$ and JEWEL. This comparison shows that PYTHIA 8 overshoots the data by 30% whereas JEWEL systematically undershoots the data by $20 - 80\%$. This preliminary comparison thus indicates that further tuning of MC generator parameters is needed.

Bibliography

[1] Dr. H. Geiger and E. Marsden . Lxi. the laws of deflexion of a particles through large angles. *The London, Edinburgh, and Dublin Philosophical Magazine and Journal of Science*, 25(148):604–623, 1913. (document)

[2] R. W. McAllister and R. Hofstadter. Elastic scattering of 188-mev electrons from the proton and the alpha particle. *Phys. Rev.*, 102:851–856, May 1956. (document)

[3] Richard E. Taylor. Deep inelastic scattering: The early years. *Rev. Mod. Phys.*, 63:573–595, Jul 1991. (document)

[4] Henry W. Kendall. Deep inelastic scattering: Experiments on the proton and the observation of scaling. *Rev. Mod. Phys.*, 63:597–614, Jul 1991. (document)

[5] Jerome I. Friedman. Deep inelastic scattering: Comparisons with the quark model. *Rev. Mod. Phys.*, 63:615–627, Jul 1991. (document)

[6] David J. Gross and Frank Wilczek. Ultraviolet behavior of non-abelian gauge theories. *Phys. Rev. Lett.*, 30:1343–1346, Jun 1973. (document)

[7] H. David Politzer. Reliable perturbative results for strong interactions? *Phys. Rev. Lett.*, 30:1346–1349, Jun 1973. (document)

[8] A. Majumder and M. Van Leeuwen. The Theory and Phenomenology of Perturbative QCD Based Jet Quenching. *Prog. Part. Nucl. Phys.*, 66:41–92, 2011. (document)

[9] Urs Achim Wiedemann. Jet Quenching in Heavy Ion Collisions. pages 521–562, 2010. [Landolt-Bornstein23,521(2010)]. (document)

[10] Günther Dissertori, Ian Knowles, and Michael Schmelling. *Quantum chromodynamics*. Oxford University Press, 2005. 1, 1.2, 1.2, 1.6

[11] Jiří Chýla. *Quarks, partons and Quantum Chromodynamics*. Accessed: 10.09.2017. 1.1, 1.1, 1.4, 1.5, 1.6, 1.5, 1.6

[12] J. Rak and M.J. Tannenbaum. *High PT Physics in the Heavy Ion Era*. Cambridge monographs on particle physics, nuclear physics, and cosmology. 2013. 1.1, 1.5, 1.6, 1.8.3

[13] Alexandre Deur, Stanley J. Brodsky, and Guy F. de Teramond. The QCD Running Coupling. *Prog. Part. Nucl. Phys.*, 90:1–74, 2016. 1.4

[14] G. M. Prosperi, M. Raciti, and C. Simolo. On the running coupling constant in QCD. *Prog. Part. Nucl. Phys.*, 58:387–438, 2007. 1.4

[15] Bethke and Siegfried. Experimental tests of asymptotic freedom. *Prog. Part. Nucl. Phys.*, 58:351–386, 2007. 1.4

[16] Ringaile Placakyte. Parton Distribution Functions. In *Proceedings, 31st International Conference on Physics in collisions (PIC 2011): Vancouver, Canada, August 28-September 1, 2011*, 2011. 1.5, 1.5

[17] D. Ebert, R. N. Faustov, and V. O. Galkin. Mass spectra and Regge trajectories of light mesons in the relativistic quark model. *Phys. Rev.*, D79:114029, 2009. 1.7

[18] C. Y. Wong. *Introduction to high-energy heavy ion collisions.* 1995. 1.6, 1.6, 1.6, 1.6

[19] Bo Andersson, G. Gustafson, M. Ringner, and P. J. Sutton. The Feynman-Wilson gas and the Lund model. *Eur. Phys. J.*, C7:251–261, 1999. 1.9

[20] Torbjorn Sjostrand, Stephen Mrenna, and Peter Z. Skands. A Brief Introduction to PYTHIA 8.1. *Comput. Phys. Commun.*, 178:852–867, 2008. 1.6, 4, 6.2, 8

[21] Gavin P. Salam. Towards Jetography. *Eur. Phys. J.*, C67:637–686, 2010. 1.7, 1.7, 1.10, 1.11, 1.12

[22] Yuri L. Dokshitzer, Valery A. Khoze, Alfred H. Mueller, and S. I. Troian. *Basics of perturbative QCD.* 1991. 1.7

[23] Toichiro Kinoshita. Mass singularities of feynman amplitudes. *Journal of Mathematical Physics*, 3(4):650–677, 1962. 1.7

[24] Matteo Cacciari, Gavin P. Salam, and Gregory Soyez. FastJet User Manual. *Eur. Phys. J.*, C72:1896, 2012. 1.7, 3.3

[25] Betty Abelev et al. Measurement of Event Background Fluctuations for Charged Particle Jet Reconstruction in Pb-Pb collisions at $\sqrt{s_{NN}} = 2.76$ TeV. *JHEP*, 03:053, 2012. 1.7

[26] Betty Abelev et al. Underlying Event measurements in pp collisions at $\sqrt{s} = 0.9$ and 7 TeV with the ALICE experiment at the LHC. *JHEP*, 07:116, 2012. 1.8

[27] Matteo Cacciari and Gavin P. Salam. Pileup subtraction using jet areas. *Phys. Lett.*, B659:119–126, 2008. 1.8

[28] Gregory Soyez. Jet areas as a tool for background subtraction. In *25th Winter Workshop on Nuclear Dynamics (WWND 2009) Big Sky, Montana, February 1-8, 2009*, 2009. 1.8, 1.8.1

[29] Serguei Chatrchyan et al. Measurement of the underlying event activity in pp collisions at $\sqrt{s} = 0.9$ and 7 TeV with the novel jet-area/median approach. *JHEP*, 08:130, 2012. 1.8, 1.8.2

[30] Betty Bezverkhny Abelev et al. Charged jet cross sections and properties in proton-proton collisions at $\sqrt{s} = 7$ TeV. *Phys. Rev.*, D91(11):112012, 2015. 1.13, 1.9

[31] B. Abelev et al. Measurement of the inclusive differential jet cross section in pp collisions at $\sqrt{s} = 2.76$ TeV. *Phys. Lett.*, B722:262–272, 2013. 1.9, 1.14

[32] Lyndon Evans and Philip Bryant. Lhc machine. *Journal of Instrumentation*, 3(08):S08001, 2008. 2.1

[33] LHC Guide. Mar 2017. 2.1

[34] Cinzia De Melis. The CERN accelerator complex. Complexe des accélérateurs du CERN. Jan 2016. General Photo. 2.1

[35] The ALICE Collaboration. The alice experiment at the cern lhc. *Journal of Instrumentation*, 3(08):S08002, 2008. 2.2

[36] *ALICE Inner Tracking System (ITS): Technical Design Report*. Technical Design Report ALICE. CERN, Geneva, 1999. 2.2.1

[37] G Dellacasa and L Ramello. *ALICE time projection chamber: Technical Design Report*. Technical Design Report ALICE. CERN, Geneva, 2000. 2.2.2

[38] P Cortese, G Dellacasa, and Ramello. *ALICE forward detectors: FMD, TO and VO: Technical Design Report*. Technical Design Report ALICE. CERN, Geneva, 2004. Submitted on 10 Sep 2004. 2.2.3, 2.3

[39] The alice offline bible. http://alice-offline.web.cern.ch/sites/alice-offline.web.cern.ch/files/uploads/OfflineBible.pdf. Accessed: 19.4.2018. 2.2.4, 3.2

[40] I. Antcheva et al. ROOT: A C++ framework for petabyte data storage, statistical analysis and visualization. *Comput. Phys. Commun.*, 180:2499–2512, 2009. 2.2.4

[41] Grid. http://alice-offline.web.cern.ch/sites/alice-offline.web.cern.ch/files/uploads/OfflineBible.pdf. Accessed: 19.4.2018. 2.2.4

[42] Rüdiger Haake. Charged Jets in Minimum Bias p-Pb Collisions at $\sqrt{s_{NN}} = 5.02$ TeV with ALICE. *PoS*, EPS-HEP2013:176, 2013. 3.2

[43] The ALICE definition of primary particles. Jun 2017. 3.2

[44] Andreas Hocker and Vakhtang Kartvelishvili. SVD approach to data unfolding. *Nucl. Instrum. Meth.*, A372:469–481, 1996. 6.1, 6.1, 6.1, 6.1, 6.1

[45] G. D'Agostini. A multidimensional unfolding method based on bayes' theorem. *Nuclear Instruments and Methods in Physics Research Section A: Accelerators, Spectrometers, Detectors and Associated Equipment*, 362(2):487 – 498, 1995. 7.1

[46] Roounfold. http://hepunx.rl.ac.uk/adye/software/unfold/RooUnfold.html. Accessed: 19.4.2018. 7.1

[47] Jaroslav Adam et al. Centrality dependence of charged jet production in p–Pb collisions at $\sqrt{s_{\mathrm{NN}}} = 5.02$ TeV. *Eur. Phys. J.*, C76(5):271, 2016. 7.4

[48] Shreyasi Acharya et al. Transverse momentum spectra and nuclear modification factors of charged particles in pp, p-Pb and Pb-Pb collisions at the LHC. 2018. 7.5

[49] Paolo Bartalini and Jochen Klein. V0and cross-section. Private communication. Accessed: 12.11.2017. 8

[50] Korinna C. Zapp. JEWEL 2.0.0: directions for use. *Eur. Phys. J.*, C74(2):2762, 2014. 8

[51] Torbjorn Sjostrand, Stephen Mrenna, and Peter Z. Skands. PYTHIA 6.4 Physics and Manual. *JHEP*, 05:026, 2006. 8